A conservative numerical scheme for modeling nonlinear acoustic propagation in thermoviscous homogeneous media

Manuel A. Diaz [a], Maxim A. Solovchuk [a,b,*], Tony W.H. Sheu [b,c]

[a] *Institute of Biomedical Engineering and Nanomedicine, National Health Research Institutes, 35053, Taiwan*
[b] *Engineering Science & Ocean Engineering Department, National Taiwan University, 10617, Taiwan*
[c] *Center of Advanced Study in Theoretical Sciences, National Taiwan University, 10617, Taiwan*

A B S T R A C T

A nonlinear system of partial differential equations capable of describing the nonlinear propagation and attenuation of finite amplitude perturbations in thermoviscous media is presented. This system constitutes a full nonlinear wave model that has been formulated in the conservation form. Initially, this model is investigated analytically in the inviscid limit where it has been found that the resulting flux function fulfills the Lax–Wendroff theorem, and the scheme can match the solutions of the Westervelt and Burgers equations numerically. Here, high-order numerical descriptions of strongly nonlinear wave propagations become of great interest. For that matter we consider finite difference formulations of the weighted essentially non-oscillatory (WENO) schemes associated with explicit strong stability preserving Runge–Kutta (SSP-RK) time integration methods. Although this strategy is known to be computationally demanding, it is found to be effective when implemented to be solved in graphical processing units (GPUs). As we consider wave propagations in unbounded domains, perfectly matching layers (PML) have been also considered in this work. The proposed system model is validated and illustrated by using one- and two-dimensional benchmark test cases proposed in the literature for nonlinear acoustic propagation in homogeneous thermoviscous media.

© 2018 Elsevier Inc. All rights reserved.

1. Introduction

The numerical description of high amplitude ultrasound propagation is a challenging and computationally intense task [1] for two main reasons. Specifically, the large spatial domain size typically required for acoustic applications and the indispensable need of high-order schemes to minimize the amount of numerical dissipation introduced by the numerical scheme.

The numerical modeling of nonlinear acoustics propagation plays an important role in the development of biomedical and engineering applications, for instance, in high intensity focused ultrasound (HIFU) for thermal ablation treatment [2], shock wave lithotripsy [3] and diagnostic ultrasound imaging [4]. For these applications the linear model is inadequate as the nonlinear effect in acoustic propagation plays the major role.

In the literature, many acoustic models have been proposed (see the recent review [5]). Arguably, the two most popular approaches for the direct modeling of nonlinear acoustic propagation are the (single sided) wave model of Khokhlov–

Zabolotskaya–Kuznetsov (KZK) and the full (double sided) wave model of Westervelt. Likewise, the most notorious numerical approaches include the direct discretization with a finite difference time domain (FDTD) scheme [6–8], the dispersion relation preserving (DPR) method [9] and the *k*-space pseudo-spectral methods [10]. More recently, Albin and collaborators [11,12] have presented viscous acoustic descriptions based on the Navier–Stokes (N–S) equations using the Fourier Continuation (FC) method. The FC method is an explicit spectral scheme for modeling the transient behavior of nonlinear hyperbolic conservation systems in long-term propagations at a reasonable cost.

All the previously mentioned schemes are shown to perform well as long as the solutions are smooth. However, in the presence of discontinuous solutions, these methods need to rely on numerical artifacts such as frequency filters to damp higher-order harmonics and avoid polluting the solution with Gibbs oscillations. By using those artifacts, the above numerical approaches increase their computational cost and/or make their implementations more involving.

Arguably, the most successful shock-capturing methods are those developed for systems of hyperbolic equations, more specifically, for conservation laws [13,14]. This realization is clearly reflected in the work of Christov and collaborators [15,16]. In their study of conservative acoustic formulations, shock structures were obtained for many one-dimensional weakly-nonlinear acoustic models using MUSCL schemes.

The acoustic explorations with second-order acoustic wave models and the full N–S system in the literature have led us to consider that an acoustic model formulated as a hyperbolic system of equations can yield simpler and artifact-free numerical descriptions of linear and nonlinear acoustics with shocks propagations in homogeneous and heterogeneous thermoviscous media. This work represents an initial step towards this goal. Like the classical thermoviscous wave models, our exploration concentrates on hyperbolic formulations to describe directly acoustic propagations as pressure wave fluctuations. For that purpose, we start by considering the finite amplitude model of Aanonsen [17] called *second-order wave equation* in [18]. Our investigation revealed that *the second-order wave equation* can lead to many suitable quasilinear hyperbolic systems. Although this was expected, it was not foreseen it could lead to a fully nonlinear formulation in conservation form. In the present work, this conservative formulation is numerically investigated for acoustic propagation in homogeneous media. In order to describe strongly nonlinear propagation, the methodology considered is based on the fifth- and seventh-order finite difference WENO reconstructions for the spatial evolution and is associated with low-storage Runge–Kutta schemes for the time integration. Acoustic wave propagation in open domains is only considered, therefore the implementation of perfect matching layers (PML) has been also taken into account to avoid unphysical reflections from the boundary of our discrete domain.

This work is organized as follows. The second-order thermoviscous acoustic wave models are reviewed in § 2. In § 3, a thermoviscous acoustic formulation as a conservative hyperbolic system of equations and its simplifications are presented. The numerical implementation of the model in homogeneous media is introduced for single and multiple dimensions in § 4. In § 5, the proposed models are validated and illustrated using one- and two-dimensional benchmark tests proposed in the literature. Lastly, concluding remarks and extensions of this work are addressed in § 6.

2. Nonlinear acoustic models

A model to describe the propagation of acoustics fluctuations through homogeneous media, under the assumptions of Newtonian, compressible, irrotational, heat conducting and viscous flow, might be obtained from the equations of fluid dynamics, namely: *the equation of mass conservation*

$$\frac{\partial \rho}{\partial t} + \nabla \cdot (\rho \boldsymbol{v}) = 0, \tag{1}$$

the equation of motion

$$\rho \left(\frac{\partial \boldsymbol{v}}{\partial t} + (\boldsymbol{v} \cdot \nabla)\boldsymbol{v} \right) = -\nabla p + \mu \nabla^2 \boldsymbol{v} + \left(\mu_B + \frac{1}{3}\mu \right) \nabla (\nabla \cdot \boldsymbol{v}), \tag{2}$$

the equation of heat transfer

$$\rho T \left(\frac{\partial s}{\partial t} + (\boldsymbol{v} \cdot \nabla)s \right) = \frac{\mu}{2} \left(\frac{\partial v_i}{\partial x_j} + \frac{\partial v_j}{\partial x_i} - \frac{2}{3}\delta_{ij} \frac{\partial v_k}{\partial x_k} \right)^2 + \mu_B (\nabla \cdot \boldsymbol{v})^2 + \kappa \nabla^2 T, \tag{3}$$

and the *equation of state (EoS)*

$$p = p(\rho, s), \tag{4}$$

where $\boldsymbol{v} : \boldsymbol{v}(\boldsymbol{x}, t) = (u(\boldsymbol{x}, t), v(\boldsymbol{x}, t), w(\boldsymbol{x}, t))$ is the fluid particle velocity, $\rho : \rho(\boldsymbol{x}, t)$ is the density of the media, $s : s(\boldsymbol{x}, t)$, the entropy, p and T are the pressure and temperature, respectively. $\boldsymbol{x} = (x, y, z) \in \mathbf{R}^3$ are the spatial (Cartesian) coordinates and $t > 0 \in \mathbf{R}$ denotes time. $\mu \geq 0$ and $\mu_B \geq 0$ are the coefficients of shear and bulk viscosity, and $\kappa \geq 0$ is the heat conductivity coefficient. The closure of the above set of equations also requires a relation between the temperature the entropy. Here, it is assumed that the temperature is a function of the density and entropy, namely

$$T = T(\rho, s).$$ (5)

The formulation of a nonlinear wave model starts by describing the acoustic propagation as small fluctuations of ρ, p, s and T from their unperturbed state, ρ_0, p_0, s_0 and T_0. This unperturbed state is assumed as fluid at rest where ρ_0, p_0, s_0 and T_0 are spatially uniform, so that any perturbation is given as

$$\begin{cases} \rho_a = \rho - \rho_0, & p_a = p - p_0, \\ s_a = s - s_0, & T_a = T - T_0. \end{cases}$$ (6)

The acoustic propagation speed, v_a, is also considered to be a small fluctuation when compared to the sound speed of the media, c_0. Using the acoustic speed, the small Mach number, ε, can be defined as $v_a/c_0 = \varepsilon \ll 1$ and used as a length scale to characterize the amplitude of the acoustic wave. Similarly, the relation $\zeta = \frac{\mu}{\rho_0 c_0 l_c}$ is used as length scale for the dissipation. Here, l_c is the characteristic length such that $l_c = c_0 t_c$ and where t_c is a characteristic time.

By introducing these relations in Eq. (6) into equations (1)–(3), a set of fluctuation equations is obtained. The order of each of the terms in the fluctuation equations can be revealed through a normalization process using the above mentioned length scales and characteristic parameters. If the terms of order ε, ε^2 and $\zeta\varepsilon$ are retained, we arrive at the set of equations

$$\frac{\partial \rho_a}{\partial t} + \rho_0 \nabla \cdot v_a = -\rho_a \nabla \cdot v_a - v_a \cdot \nabla \rho_a,$$ (7)

$$\rho_0 \frac{\partial v_a}{\partial t} + \nabla p_a = \left(\mu_B + \frac{4}{3}\mu\right) \nabla^2 v_a - \rho_a \frac{\partial v_a}{\partial t} - \rho_0 (v_a \cdot \nabla) v_a,$$ (8)

$$\rho_0 T_0 \frac{\partial s_a}{\partial t} = \kappa \nabla^2 T_a,$$ (9)

which can be used to describe the propagation of acoustics fluctuations through homogeneous media. In this step, the viscosity coefficients μ and μ_B, and the heat coefficient κ have been treated also as small fluctuating quantities. Equations (7), (8) and (9) then constitute a set of equations that is consistent up to the second-order (ε, ε^2, $\zeta\varepsilon$) [19].

The normalization process indicates that s_a is order $\zeta\varepsilon$, therefore, it is customary to assume the EoS as a truncated Taylor expansion around the values ρ_0 and s_0 of the form,

$$p = p|_{\rho_0, s_0} + \rho_a \left.\frac{\partial p}{\partial \rho}\right|_{s_0, \rho_0} + \frac{\rho_a^2}{2} \left.\frac{\partial^2 p}{\partial \rho^2}\right|_{s_0, \rho_0} + s_a \left.\frac{\partial p}{\partial s}\right|_{s_0, \rho_0} + O(\varepsilon^3, \zeta\varepsilon^2),$$

and the temperature relation as a first-order Taylor expansion, namely

$$t = t|_{\rho_0, s_0} + \rho_a \left.\frac{\partial t}{\partial \rho}\right|_{s_0, \rho_0} + O(\varepsilon\zeta, \varepsilon^2).$$

Using the ideal gas thermodynamic relations, Eq. (9), and the first-order expansion of the temperature relation yields the equation of state for thermoviscous propagations [19], namely

$$p_a = c_0^2 \rho_a + \frac{c_0^2}{\rho_0} \frac{B/A}{2} \rho_a^2 + \frac{\kappa}{\rho_0} \left(\frac{1}{c_v} - \frac{1}{c_p}\right) \frac{\partial \rho_a}{\partial t},$$ (10)

where the factor B/A is the media's *coefficient of nonlinearity*, c_v and c_p are the media's heat capacities at constant volume and pressure, respectively. It is also customary to introduce the *Lagrangian energy density*

$$\mathcal{L} = E_c - E_p = \frac{1}{2}\rho_0 (v_a \cdot v_a) - \frac{p_a^2}{2\rho_0 c_0^2},$$ (11)

which allows to reformulate the RHS of equation (7) and (8) as

$$\rho_0 \frac{\partial v_a}{\partial t} + \nabla p_a = \left(\mu_B + \frac{4}{3}\mu\right) \nabla^2 v_a - \nabla \mathcal{L},$$ (12a)

$$\frac{\partial \rho_a}{\partial t} + \rho_0 \nabla \cdot v_a = \frac{1}{\rho_0 c_0^4} \frac{\partial p_a^2}{\partial t} + \frac{1}{c_0^2} \frac{\partial \mathcal{L}}{\partial t}.$$ (12b)

2.1. The second-order wave equation

Aanonsen and collaborators [17] recognized that Eqs. (12) along with the EoS, Eq. (10), can be the basic building blocks for the formulation of a second-order description of the thermoviscous acoustic propagation. By combining these equations into a single wave model, Aanonsen obtained

$$\nabla^2 p_a - \frac{1}{c_0^2}\frac{\partial^2 p_a}{\partial t^2} = -\frac{\mathcal{D}}{c_0^4}\frac{\partial^3 p_a}{\partial t^3} - \frac{\beta}{\rho_0 c_0^4}\frac{\partial^2 p_a^2}{\partial t^2} - \left(\nabla^2 + \frac{1}{c_0^2}\frac{\partial^2}{\partial t^2}\right)\mathcal{L}, \tag{13}$$

where $\nabla^2 = \nabla \cdot \nabla$ is the Laplace operator, $\beta = 1 + \frac{B}{2A}$ is now the quadratic parameter of nonlinearity and

$$\mathcal{D} = \frac{1}{\rho_0}\left(\mu_B + \frac{4}{3}\mu\right) + \frac{\kappa}{\rho_0}\left(\frac{1}{c_v} - \frac{1}{c_p}\right)$$

is *Lighthill's acoustic diffusivity*. This result has been termed in [18] as the *second-order wave equation*. Moreover, written in this form, one can recognize in this model that it is composed of the linear wave equation of a progressive wave on the LHS, while on the RHS, the first term is responsible for the inclusion of *absorption* (diffusion) of the media into the propagation. The second term on the RHS is known to produce the cumulative nonlinear effects on the waveform along the propagation, while the last term is responsible for the *local nonlinear effects* of the waveform.

2.2. The Westervelt model

One of the known difficulties of dealing with Eq. (13) is an explicit formulation of the Lagrangian rate of change. Hamilton and Blackstock have provided an indirect way of performing this formulation in [18]. However, when *local nonlinear effects* are negligible, i.e. $\mathcal{L} = 0$, and only *nonlinear cumulative effects* take place along the propagation. The Lagrangian energy density equation (11) indicates that

$$|p_a| = \rho_0 c_0 |u_a|, \tag{14}$$

which is traditionally termed *the linear impedance relation*. As a result, the Westervelt model [20] is recovered, namely

$$\nabla^2 p_a - \frac{1}{c_0^2}\frac{\partial^2 p_a}{\partial t^2} = -\frac{\mathcal{D}}{c_0^4}\frac{\partial^3 p_a}{\partial t^3} - \frac{\beta}{\rho_0 c_0^4}\frac{\partial^2 p_a^2}{\partial t^2}. \tag{15}$$

The Westervelt equation, like the *second-order wave equation*, is a full wave model, e.g. if the model is limited to a single dimension, it simply becomes a two-wave model. Moreover, the analysis of the single-side propagation [18, chap. 3.7] from the Westervelt equation has been shown to recover the classical Burgers' equation [21].

The elegance of the equation model (15) is that it is capable of describing acoustic thermoviscous propagation by simply evolving a single scalar pressure field. However, from the numerical perspective, the discretization techniques of this model are hindered by the high-order time derivative terms. In the literature it is customary to use a finite difference time discrete (FDTD) scheme, or a Fourier-type spectral scheme to solve discretely for the Westervelt equation (15). Although these techniques are enough to model weakly nonlinear propagation (smooth nonlinear propagation), the description of strongly nonlinear wave propagations (nonlinear propagations where shocks have already developed) still remains a challenging task.

Arguably the most successful schemes for capturing steepening profiles (or discontinuous solutions) are the shock capturing schemes developed for hyperbolic system of equations [13,14]. Therefore, it would be desirable to formulate equations model (13) and/or (15) into a suitable form that can make use of shock-capturing strategies. In this work we consider this idea seriously as we pursue an acoustic formulation as hyperbolic system of equations in the following section.

3. Thermoviscous hyperbolic acoustic system

Let us start our development by considering equations in (12) as an intermediate step. The temporal derivative of the acoustic density $\frac{\partial \rho_a}{\partial t}$ using the EoS can be written in the following form [18]

$$\frac{\partial \rho_a}{\partial t} = \frac{1}{c_0^2}\frac{\partial p_a}{\partial t} - \frac{B/A}{2\rho_0 c_0^4}\frac{\partial p_a^2}{\partial t} - \frac{\kappa}{\rho_0 c_0^2}\left(\frac{1}{c_v} - \frac{1}{c_p}\right)\nabla^2 p_a, \tag{16}$$

so that substituting this last result in (12) yields

$$\rho_0\frac{\partial \boldsymbol{v}_a}{\partial t} + \nabla p_a = \left(\mu_B + \frac{4}{3}\mu\right)\nabla^2 \boldsymbol{v}_a - \nabla\mathcal{L}$$

$$\frac{1}{c_0^2}\frac{\partial p_a}{\partial t} + \rho_0\nabla \cdot \boldsymbol{v}_a = \frac{\beta}{\rho_0 c_0^4}\frac{\partial p_a^2}{\partial t} + \frac{\kappa}{\rho_0 c_0^2}\left(\frac{1}{c_v} - \frac{1}{c_p}\right)\frac{\partial^2 p_a}{\partial t^2} + \frac{1}{c_0^2}\frac{\partial\mathcal{L}}{\partial t}. \tag{17}$$

To write this system in a hyperbolic system, it is necessary to write the nonlinear β-term in a more suitable form. From first-order relations, the nonlinear term can be re-expressed as $\frac{1}{\rho_0 c_0^2} \frac{\partial p^2}{\partial t} = -2p_a \nabla \cdot \boldsymbol{v}_a + O(\varepsilon^3)$ [10] yielding

$$\frac{\partial \boldsymbol{v}_a}{\partial t} + \frac{1}{\rho_0} \nabla p_a = \frac{1}{\rho_0} \left(\mu_B + \frac{4}{3}\mu \right) \nabla^2 \boldsymbol{v}_a - \frac{\nabla \mathcal{L}}{\rho_0},$$

$$\frac{\partial p_a}{\partial t} + (c_0^2 \rho_0 + 2\beta p_a) \nabla \cdot \boldsymbol{v}_a = \frac{\kappa}{\rho_0} \left(\frac{1}{c_v} - \frac{1}{c_p} \right) \nabla^2 p_a + \frac{\partial \mathcal{L}}{\partial t},$$

(18)

where

$$\begin{cases} \frac{\nabla \mathcal{L}}{\rho_0} = (\boldsymbol{v}_a \cdot \nabla)\boldsymbol{v}_a - \frac{1}{(\rho_0 c_0)^2} p_a \nabla p_a, \\ \frac{\partial \mathcal{L}}{\partial t} = \frac{\rho_0}{2} \frac{\partial}{\partial t} (\boldsymbol{v}_a \cdot \boldsymbol{v}_a) - \frac{1}{2\rho_0 c_0^2} \frac{\partial}{\partial t} (p_a^2). \end{cases}$$

(19)

This hyperbolic system is an exact reformulation of the second-order Eq. (13) as no extra assumption has been made. However, in contrast to Eq. (13), it provides a direct way to evaluate the Lagrangian energy density. When written in the vector from, the system in Eq. (18) has the form

$$\boldsymbol{q}_t + A\nabla \cdot \boldsymbol{q} = \psi(\boldsymbol{q}).$$

(20)

This is a quasilinear hyperbolic formulation that can be numerically approached by Leveque's *wave fluctuations* methods [13] to model ultrasound propagation for Biomedical applications [2–4]. However, modeling the propagation of ultrasound waves for Biomedical purposes under Eq. (18) can be computationally demanding as the propagation of such waves is mostly dominated by *cumulative nonlinear effects* while the contribution of *local nonlinear effects* is negligible [10]. Therefore it is desirable to introduce some simplifications to the model (18).

3.1. A conservative formulation

Aanonsen et al. in [17] have shown that neglecting the contribution of *local nonlinear effects* is equivalent to neglecting the contribution of the Lagrangian energy density terms by setting $\mathcal{L} = 0$. Moreover, in this work, it is found that under this condition the nonlinear derivative in the β-term can also be approximated as $\frac{1}{\rho_0 c_0^2} \frac{\partial (p_a^2)}{\partial t} = -\nabla \cdot (p_a \boldsymbol{v}_a) + O(\varepsilon^3)$ (refer to Appendix B section for details), so that the system in Eqs. (17), becomes

$$\frac{\partial \boldsymbol{v}_a}{\partial t} + \frac{1}{\rho_0} \nabla p_a = \frac{1}{\rho_0} \left(\mu_B + \frac{4}{3}\mu \right) \nabla^2 \boldsymbol{v}_a,$$

$$\frac{\partial p_a}{\partial t} + \nabla \cdot \left((c_0^2 \rho_0 + \beta p_a) \boldsymbol{v}_a \right) = \frac{\kappa}{\rho_0} \left(\frac{1}{c_v} - \frac{1}{c_p} \right) \nabla^2 p_a,$$

(21)

which can be expressed as a conservative hyperbolic system of the form $\boldsymbol{q}_t + \nabla \cdot \boldsymbol{f}(\boldsymbol{q}) = \psi(\boldsymbol{q})$. In principle, this nonlinear system should be consistent with the Westervelt equation and be able to describe the propagation of *progressive waves* in the sense of [18]. Moreover, in the lossless scenario, $\kappa = \mu_B = \mu = 0$, this set of equations becomes a conservative hyperbolic system of the form

$$\frac{\partial \boldsymbol{v}_a}{\partial t} + \frac{1}{\rho_0} \nabla p_a = 0,$$

$$\frac{\partial p_a}{\partial t} + \nabla \cdot \left((c_0^2 \rho_0 + \beta p_a) \boldsymbol{v}_a \right) = 0,$$

(22)

that generalizes the *linear acoustics system* of equations ($\beta = 0$). Because of this fact, we will refer to it as the *nonlinear acoustic system* (NAS) of equations.

In this work, Eq. (21) is a thermoviscous conservative hyperbolic system of equations that directly describes the propagation of an acoustics perturbation as a pressure wave fluctuation. To the best of the author's knowledge, this conservative hyperbolic system and its simplifications have not been reported before.

From the numerical implementation perspective, it is evident that the main difficulty in using Eq. (21) lies in solving discretely the NAS equations, given that its nonlinear nature of the flux function, $\boldsymbol{f}(\boldsymbol{q})$, could give rise to discontinuities in the solution. Therefore, the properties and numerical challenges imposed by the system in Eq. (22) need to be initially investigated before addressing the conservative thermoviscous model.

The present study concentrates on applications with ultrasound propagation under the assumption of *progressive waves*. Therefore, acoustic propagation in thermoviscous media is here only considered under the model in Eq. (21), since the contribution of *local nonlinear effects* in progressive waves is considered negligible [18]. However, an investigation of their contributions will be explored in the future expansion of the present work.

Remark. Like the traditional second-order thermoviscous wave equations, the conservative thermoviscous formulation approximates the N–S hydrodynamic equations (or Euler equations in the inviscid limit). From the numerical perspective, the advantage of the present thermoviscous formulation over the hydrodynamic equations is attributed to the fact that we are solving directly for hydrodynamic acoustic quantities (p_a, $\boldsymbol{v}_a$) while using the hydrodynamic equations, and the acoustic fluctuations are addressed indirectly from the macroscopic hydrodynamic quantities (ρ, $\boldsymbol{v}$, p).

Remark. The sub-index "a" is kept throughout this presentation as a reminder that these hydrodynamic quantities represent acoustic fluctuations which, unlike in the case classical equations of gas dynamics, are not restricted to only positive values.

3.2. One-dimensional analysis

The *nonlinear acoustic system* in a single spatial dimension takes the form

$$\frac{\partial u_a}{\partial t} + \frac{1}{\rho_0}\frac{\partial p_a}{\partial x} = 0,$$
$$\frac{\partial p_a}{\partial t} + \frac{\partial\left((c_0^2\rho_0 + \beta p_a)u_a\right)}{\partial x} = 0. \tag{23}$$

Using vector notation the above system can be simply recast as

$$\boldsymbol{q}_t + \boldsymbol{f}(\boldsymbol{q})_x = 0, \tag{24}$$

where $\boldsymbol{q}$ and $\boldsymbol{f}(\boldsymbol{q})$ are now defined as

$$\boldsymbol{q} = \begin{bmatrix} u_a \\ p_a \end{bmatrix} = \begin{bmatrix} q^{(1)} \\ q^{(2)} \end{bmatrix}, \qquad \boldsymbol{f}(\boldsymbol{q}) = \begin{bmatrix} q^{(2)}/\rho_0 \\ (\rho_0 c_0^2 + \beta q^{(2)})q^{(1)} \end{bmatrix}. \tag{25}$$

From the principle of hyperbolicity, the Jacobian matrix

$$A = \frac{\partial \boldsymbol{f}}{\partial \boldsymbol{q}} = \begin{bmatrix} \frac{\partial f_1}{\partial q_1} & \frac{\partial f_1}{\partial q_2} \\ \frac{\partial f_2}{\partial q_1} & \frac{\partial f_2}{\partial q_2} \end{bmatrix} = \begin{bmatrix} 0 & 1/\rho_0 \\ \rho_0 c_0^2 + \beta q_2 & \beta q_1 \end{bmatrix}, \tag{26}$$

might be expressed as

$$A = R\Lambda R^{-1} \tag{27}$$

where $\Lambda = diag(\lambda_1, \lambda_2)$ is a diagonal matrix and R is the matrix of the right eigenvector. For the nonlinear system (23), the eigenvalues are found to be

$$\lambda_{1,2} = \frac{1}{2}\left(\beta u_a \mp \sqrt{4c_0^2 + 4\beta p_a/\rho_0 + \beta^2 u_a^2}\right), \tag{28}$$

and their corresponding vectors are

$$R = [\boldsymbol{r}_1, \boldsymbol{r}_2] = \begin{bmatrix} -\frac{c_0 + \frac{\beta}{2}(\frac{p_a}{\rho_0 c_0} + u_a)}{\rho_0 c_0^2 + \beta p_a} & \frac{c_0 + \frac{\beta}{2}(\frac{p_a}{\rho_0 c_0} - u_a)}{\rho_0 c_0^2 + \beta p_a} \\ 1 & 1 \end{bmatrix}. \tag{29}$$

Written in this form, the meaning of this structure is not clear. Some meanings can be easily recovered under the assumption of $\mathcal{L} = 0$, so that by means of the square form of the linear acoustics impedance relation, $u_a^2 = \left(\frac{p_a}{\rho_0 c_0}\right)^2$, the argument in the radical of the eigenvectors can then be recognized as the squared binomial $(2c_0 + \beta p_a/(\rho_0 c_0))^2$. As a result, we further simplify the above expression as

$$\lambda_1 = -c_0 + \frac{\beta}{2}\left(u_a - \frac{p_a}{\rho_0 c_0}\right), \quad \lambda_2 = c_0 + \frac{\beta}{2}\left(\frac{p_a}{\rho_0 c_0} + u_a\right). \tag{30}$$

In this form, it is easy to realize that the eigenvalues are different and real, meaning that the system (23) is *strictly hyperbolic*. It is noted that both results can be further simplified by taking into account the vector nature of the linear impedance relation. Numerical experience shows that the wave magnitudes $|p_a|$ and $|u_a|$ are related. Again, if $\mathcal{L} = 0$ holds true, we can use the linear impedance relation so that $|p_a|$ and $|u_a|$ for the forward propagation are related as $u_a = p_a/(\rho_0 c_0)$, while for backward propagation they become $u_a = -p_a/(\rho_0 c_0)$. Substituting for u_a in Eqs. (30) yields

$$\begin{cases} \lambda_1 = -\left(c_0 + \frac{\beta p_a}{\rho_0 c_0}\right), & \text{for a backward propagation and} \\ \lambda_2 = \quad c_0 + \frac{\beta p_a}{\rho_0 c_0}, & \text{for a forward propagation,} \end{cases} \tag{31}$$

this also indicates that the accumulation of nonlinear effects takes place in the direction along which they propagate. Eqs. (30) also show that the conservative system remains strictly hyperbolic as the magnitudes remain real and distinct. It is evident that under the linear limit ($\beta = 0$), the eigenvalues will simply reduce to $\lambda_1 = -c_0$ and $\lambda_2 = c_0$. The same is true for the eigenvalues in the Eq. (30). Although the analysis of expressions in Eq. (28) is more complex than that of Eq. (31) the conclusion will be the same as long as $(|p_a/\rho_0|, |u_a^2|) < |c_0^2|$.

Remark. For planar and progressive waves, it is well accepted that the *linear impedance relation* holds true since $\mathcal{L} = 0$ [18]. Here, this assumption is used in our discussion to acquire some meaning from the eigenstructure of the 1-d NAS system. Notice, however, that a propagation described by this model is more general than that of a progressive wave. The eigenstructure presented in Eqs. (28) and (29) indicates that the NAS model can describe propagations in linear as well as nonlinear regimes regardless of any assumption on whether *local nonlinear effects* are taken into account or whether the *linear impedance relation* holds or not in the propagation.

3.3. Lax entropy analysis

A shock structure obtained in Eq. (23) separates two constant states and propagates at velocity υ. At this level, the Rankine–Hugoniot jump condition,

$$[\boldsymbol{f}(\boldsymbol{q}) - \upsilon \boldsymbol{q}]_r^l = \boldsymbol{f}(\boldsymbol{q}_r) - \boldsymbol{f}(\boldsymbol{q}_l) - \upsilon(\boldsymbol{q}_r - \boldsymbol{q}_l) = 0, \tag{32}$$

must hold. Here $\boldsymbol{q}_r$ and $\boldsymbol{q}_l$ denote the constant states to the right and left of the shock. The shock propagation is then measured in a fixed coordinate system. Hence υ is not changed across the shock.

It is well-known that the Rankine–Hugoniot jump condition admits many non-physical solutions. For physically real applications, the Lax entropy condition states that for the correct solution there is an index j such that

$$\lambda_j(\boldsymbol{q}_l) > \upsilon > \lambda_j(\boldsymbol{q}_r). \tag{33}$$

Recall that $\lambda_j(\boldsymbol{q})$ are the wave speeds for the propagation of a small amplitude signal, linearized about the state $\boldsymbol{q}$. That is, $\lambda_j(\boldsymbol{q})$ is equivalent to the local speed of sound. Hence the Lax entropy condition states that the shock propagation velocity is supersonic with respect to the fluid ahead of the shock, and subsonic with respect to the fluid behind it.

For Eq. (23), using the short notation of the Eq. (32), the Rankine–Hugoniot relation takes the form

$$[p_a/\rho_0 - \upsilon u_a]_l^r = 0, \tag{34}$$

$$[(c_0^2 \rho_0 + \beta p_a)u_a - \upsilon p_a]_l^r = 0. \tag{35}$$

By setting initially the acoustics quantities to the right side of the shock into a quiescent state, i.e. set $p_{a,r} = 0$ and $u_{a,r} = 0$, the resulting expression can be combined into a single expression by eliminating $u_{a,l}$ from them. Solving the resulting expression for the shock velocity yields

$$\upsilon = \pm c_0 \sqrt{1 + \frac{\beta p_{a,l}}{\rho_0 c_0^2}} \approx \pm \left(c_0 + \frac{1}{2} \frac{\beta p_{a,l}}{\rho_0 c_0}\right). \tag{36}$$

If instead, we choose to eliminate $p_{a,l}$ and solve the characteristic values of the shock structures, the alternative expression

$$\upsilon = \frac{1}{2}\left(\beta u_{a,l} \pm \sqrt{\beta^2 u_{a,l}^2 + 4c_0^2}\right), \tag{37}$$

is obtained. Similar expressions can be also obtained in the consideration of a quiescent state to the left side of shock. When comparing results in equations (36) and (36) with the eigenvalues of the system (23), one observes that the Lax entropy condition is fulfilled which ensures that structures will remain physically meaningful.

4. Numerical implementation

Describing numerically acoustic propagations with the NAS equations requires a high-resolution solver capable of dealing with discontinuous solutions. Moreover, as we target strongly nonlinear propagation, the number of points per wavelength required can yield a large computational domain. To obtain solutions in reasonable time, an explicit algorithm implemented using a high-performance computational (HPC) solution is desirable.

Given the numerical challenges posed by the NAS equations, a finite difference method based on weighted essentially non-oscillatory (WENO) reconstructions and low-storage Runge–Kutta time integration schemes is chosen to investigate the
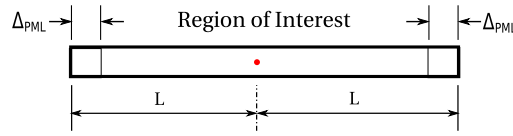
Fig. 1. One-dimensional model. The red dot indicates the origin on the reference frame. (For interpretation of the references to color in this figure legend, the reader is referred to the web version of this article.)

proposed conservative acoustic formulation in strongly nonlinear regimes with shocks. This approach provides a high-order shock-capturing scheme so that direct solutions of the *nonlinear acoustic system* and *thermoviscous acoustic system* equations can be obtained. Although this numerical strategy is well-known to be computationally demanding, the resulting schemes are fully explicit and the memory storage requirement per iteration is small when compared to a finite difference time domain discretization, which makes them suitable to be implemented and solved on general purpose graphical processing units (GPGPUs).

In this section, the discretization of one- and two-dimensional formulations of the NAS equations in Cartesian and axisymmetric coordinates, are presented. For reasons that will become evident later on, the modifications required for introducing perfectly matching layers at the boundaries, as well as discrete acoustic source terms are also delineated. The discretizations are performed in a dimensional form, i.e., keeping the physical units of the model. This is done, as it is customary in acoustics, in order to be able to compare any numerical results directly with the experimental measurements.

4.1. One-dimensional formulations

4.1.1. Cartesian formulation

Let us consider a one-dimensional initial value problem (IVP) of the form

$$
\begin{cases}
\text{PDEs:} & \boldsymbol{q}_t + \boldsymbol{f}(\boldsymbol{q})_x = 0, & x \in \Omega \in [-L, L],\ t > 0, \\
\text{ICs:} & \boldsymbol{q}(x, 0) = \boldsymbol{q}_0(x), & x \in \Omega, \\
\text{BCs:} & \boldsymbol{q}(x, t) = \boldsymbol{0}, & x \in \partial\Omega,\ t > 0,
\end{cases}
\tag{38}
$$

where $\boldsymbol{q}$ and $\boldsymbol{f}(\boldsymbol{q})$ are defined as in Eq. (25). Here, the proposed initial value problem would model the nonlinear propagation of $\boldsymbol{q}_0(x)$ over the bounded domain $\Omega \in [-L, L]$. In this model, if an incident wave interacts with either of the left or right boundaries, this wave would be reflected back into the domain. To study waves in free-flow like conditions, it is required to surround the computational domain by a non-zero width layer in which the incident waves should decay. This layer must also produce as weak as possible reflections at the interface with the region of interest. The problem under investigation is depicted in Fig. 1. In these layers, the Perfect Matching Layer approach [22] is used and its width is simply denoted Δ_{PML}. Therefore, the computational domain is subdivided into regions, namely the *region of interest* and the *PML regions*. It is evident that inside the region of interest we are interested in solving for Eq. (23). However in the PML regions, we modify the governing system of equations as

$$
\text{PML-1d:} \quad
\begin{cases}
\frac{\partial}{\partial t}(u_a) + \frac{1}{\rho_0}\frac{\partial}{\partial x}(p_a) = -\sigma_x(x)u_a, \\
\frac{\partial}{\partial t}(p_a) + \frac{\partial}{\partial x}(k_a u_a) = -\sigma_x(x)p_a,
\end{cases}
\tag{39}
$$

where $\sigma_x(x)$ is an absorption coefficient which is defined in Appendix C and k_a represents the deviation of the equilibrium state of acoustic pressure from the linear model, namely $k_a = c_0^2 \rho_0 + \beta p_a$.

4.1.2. Axisymmetric formulation

In the present work, we have also considered the case of a nonlinear acoustic propagation under azimuthal symmetry, i.e. an axisymmetric formulation of the nonlinear acoustic system. This formulation is obtained by considering the vector operators in cylindrical coordinates and neglecting the contributions of any rate of change along the azimuthal and vertical axes, namely

$$
\begin{cases}
\nabla\phi = \frac{\partial\phi}{\partial r}, \\
\nabla \cdot \boldsymbol{v} = \frac{1}{r}\frac{\partial r v_r}{\partial r}.
\end{cases}
\tag{40}
$$

Substituting the above operators into Eqs. (22) the axisymmetric formulation simply becomes

$$
\text{axisymmetric:} \quad
\begin{cases}
\frac{\partial}{\partial t}(u_a) + \frac{1}{\rho_0}\frac{\partial}{\partial r}(p_a) = 0, \\
\frac{\partial}{\partial t}(p_a) + \frac{\partial}{\partial r}(k_a u_a) = -\frac{k_a u_a}{r}.
\end{cases}
\tag{41}
$$
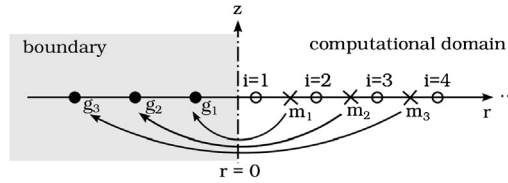
Fig. 2. Implementation of an ideal axisymmetric boundary conditions. The inner grid points $i = 1, 2, 3, \ldots$ are expanded with three outer ghost points g_1, g_2, g_3 values of which are determined by the corresponding mirror points m_1, m_2, m_3 across the axis of symmetry, $r = 0$.

Through this formulation it is easy to extend the Cartesian formulation into an axisymmetric formulation since at first glance they only differ in the radial correction term of flux $-\frac{k_a u_a}{r}$. Notice we must change the frame of reference from $x \in [-L, L]$ to $r \in [0, R]$, and enforce the following at the origin of the r-domain

$$\left. \frac{\partial \boldsymbol{f}(\boldsymbol{q})}{\partial r} \right|_{r=0} = \boldsymbol{0}. \tag{42}$$

Discretely enforcing this condition across the singularity that occurs at $r = 0$ is a simple but delicate step. Under the assumption of a central finite-difference discretization acting on a uniformly distributed grid, the discrete implementation of an ideal axisymmetric boundary condition (BC) is considered by extending the numerical grid with a finite number of ghost nodes. In Fig. 2, we exemplify the implementation of this boundary using three ghost nodes (index g). The data of p_a and u_a associated to the ghost points can be obtained from the data associated to mirror points (index m) across the axis of symmetry. In principle, the data associated to the mirror points can be obtained from interpolating the data associated to the nearby i-nodes. However, if the axis of symmetry is set to be exactly in the middle of the way of node $i = 1$ and node g_1, the data associated with the ghost point can be simply computed as

$$\text{axisymmetric BC:} \quad (p_a, u_a)_{g_i} = (p_a, -u_a)_i \,. \tag{43}$$

Using this simple strategy, one can ensure that flux across the axis of symmetry ($r = 0$) is zero without any extra computation. Moreover, the high-order scheme is applicable through the whole computational domain, so that the quality of the numerical method remains the same at the boundary and in the inner region. Alternatively, if the node $i = 1$ is set to coincide with the axis of symmetry of the domain, the values of p_a and u_a ghost cells are simply calculated as

$$\text{axisymmetric BC:} \quad (p_a, u_a)_{g_i} = (p_a, -u_a)_{i+1} \,. \tag{44}$$

Again this strategy makes the spatial derivatives associated of the flux function become zero and does not require any modification of the high-order scheme. However, let us remark that the term $-(k_a u_a)/r$ in Eq. (41) is also part of the flux function $\boldsymbol{f}(\boldsymbol{q})$ and should be dropped when evaluating discretely the radial flux derivative, $\frac{\partial}{\partial r} \boldsymbol{f}(\boldsymbol{q})$, at cell $i = 1$ ($r = 0$). So that condition in Eq. (42) is correctly fulfilled. In this work, we will always make the first node of our radial discretization to coincide with the axis of symmetry.

4.1.3. Formulation with forcing term

We are interested in introducing and studying the evolution of a harmonic signal under the NAS governing equations. This is achieved here by introducing a harmonic point source into the mass equation, so that the system becomes

$$\text{NAS + forcing term:} \quad \begin{cases} \frac{\partial}{\partial t}(u_a) + \frac{1}{\rho_0} \frac{\partial}{\partial x}(p_a) = 0, \\ \frac{\partial}{\partial t}(p_a) + \frac{\partial}{\partial x}(k_a u_a) = c_0 P_0 \, \exp(+i\omega t)\delta(x - x^*), \end{cases} \tag{45}$$

where $\delta(x)$ is the Dirac delta function given in m^{-1} units, x^* is a discrete point x^* that may or may not coincide with a discrete point in the domain, P_0 is the amplitude of the signal given in MPa and ω is the angular frequency of the harmonics signal given in rad/s. Notice that transforming back the nonlinear term to a time derivative form and partially deriving the momentum and mass equation with respect to space and time, respectively. The system is found to be consistent with the forced version of Westervelt equation, namely

$$\frac{\partial^2 p_a}{\partial r^2} - \frac{1}{c_0^2} \frac{\partial p_a}{\partial t} = -\frac{\beta}{\rho_0 c_0^4} \frac{\partial^2 p_a^2}{\partial t^2} - P_0 \frac{\omega}{c_0} \exp(+i\omega t)\delta(x - x^*). \tag{46}$$

Under the finite difference approach, modeling an acoustic point source inside a discrete domain is done by considering a discrete version of $\delta(x)$, namely $\delta_{\Delta x}^{\{M,S\}}(x)$, defined as

$$\delta_{\Delta x}^{\{M,S\}}(x_i - x^*) = \frac{1}{\Delta x} \varphi^{\{M,S\}} \left(\frac{x_i - x^*}{\Delta x} \right) \tag{47}$$

Table 1
Coefficients for the fourth-order, LSERK method.

i	a_i	b_i	c_i
1	0	$\dfrac{1432997174477}{9575080441755}$	0
2	$-\dfrac{567301805773}{1357537059087}$	$\dfrac{5161836677717}{13612068292357}$	$\dfrac{1432997174477}{9575080441755}$
3	$-\dfrac{2404267990393}{2016746695238}$	$\dfrac{1720146321549}{2090206949498}$	$\dfrac{2526269341429}{6820363962896}$
4	$-\dfrac{3550918686646}{2091501179385}$	$\dfrac{3134564353537}{4481467310338}$	$\dfrac{2006345519317}{3224310063776}$
5	$-\dfrac{1275806237668}{842570457699}$	$\dfrac{2277821191437}{14882151754819}$	$\dfrac{2802321613138}{2924317926251}$

where Δx is the spacing of a uniformly distributed grid, i is the nodes index, and $\varphi^{\{M,S\}}$ is a grid function that fulfills M-moments and S-smoothness conditions. In this work we consider the grid functions $\varphi^{\{2,0\}}$, $\varphi^{\{2,2\}}$, $\varphi^{\{4,4\}}$ and $\varphi^{\{6,6\}}$ presented in [23].

4.1.4. Temporal discretization

Written in vector notation, the formulations in equations (39), (41) and (45), can all be simply expressed in semi-discrete form as

$$\frac{\partial \boldsymbol{q}}{\partial t} = -\boldsymbol{f}(\boldsymbol{q})_x + \mathcal{S}(\boldsymbol{q}, x, t) = \mathrm{L}(\boldsymbol{q}), \tag{48}$$

where $\mathrm{L}(\boldsymbol{q})$ represents the contribution of the convective operator and source terms $\mathcal{S}(\boldsymbol{q}, x, t)$. In this form, a time integration scheme such as the strong stability preserving (SSP) third-order explicit Runge–Kutta (SSP-RK3) [24] can be simply implemented as

$$\begin{aligned}
\boldsymbol{q}^{(1)} &= \boldsymbol{q}^n + \Delta t\, \mathrm{L}(\boldsymbol{q}^n), \\
\boldsymbol{q}^{(2)} &= \frac{3}{4}\boldsymbol{q}^n + \frac{1}{4}\boldsymbol{q}^{(1)} + \frac{1}{4}\Delta t\, \mathrm{L}(\boldsymbol{q}^{(1)}), \\
\boldsymbol{q}^{n+1} &= \frac{1}{3}\boldsymbol{q}^n + \frac{2}{3}\boldsymbol{q}^{(2)} + \frac{2}{3}\Delta t\, \mathrm{L}(\boldsymbol{q}^{(2)}).
\end{aligned} \tag{49}$$

Another useful, although is not SSP, scheme is the fourth-order low-storage explicit Runge–Kutta (LSERK) [25]. This five-stage scheme is

$$\begin{aligned}
\boldsymbol{p}^{(0)} &= \boldsymbol{q}^n, \\
i \in [1, \ldots, 5] : &\begin{cases} \boldsymbol{k}^{(i)} = a_i \boldsymbol{k}^{i-1} + \Delta t\, \mathrm{L}(\boldsymbol{p}^{(i-1)}, t^n + c_i \Delta t) \\ \boldsymbol{p}^{(i)} = \boldsymbol{p}^{(i-1)} + b_i \boldsymbol{k}^{(i)}, \end{cases} \\
\boldsymbol{q}^{n+1} &= \boldsymbol{p}^{(5)},
\end{aligned} \tag{50}$$

where the coefficients a_i, b_i and c_i needed are given in Table 1.

In Section 5, only these two Runge–Kutta schemes will be mainly used in our numerical tests. For simplicity, the third-order explicit Runge–Kutta scheme will be referred to as "RK3" while the fourth-order, five-stages, Runge–Kutta scheme will be referred to as "RK4(5)".

4.1.5. Spatial discretization

In this section, a traditional finite difference approach is applied to formulate an approximation to the spatial operators on a discrete domain Ω_h within which as mesh of nodes $\cdots < x_1 < x_2 < x_3 < \cdots$ is uniformly distributed such that the spacing between contiguous nodes, $\Delta x = x_{i+1} - x_i$, is a constant. Therefore the physical location of every node is simply defined as $x_i = i\Delta x$ and the values associated to each i-node of a given function $u(x)$ are defined as $u_i = u(x_i)$.

As pointed out early, we require a higher-order method capable of dealing with discontinuities in the solution as they arise. Therefore the classical WENO discretization of Jiang and Shu [26] has been selected to approximate $\boldsymbol{f}(\boldsymbol{q})_x$ at x_i. Here, we simply give a brief presentation of the essential elements of the method.

The traditional spatial finite difference discretization of the convective operator requires the enforcement of a conservative scheme, therefore the convective operator is written as

$$\boldsymbol{f}(\boldsymbol{q})_x|_{x_i} \approx \frac{1}{\Delta x}\left(\hat{\boldsymbol{f}}_{i+\frac{1}{2}} - \hat{\boldsymbol{f}}_{i-\frac{1}{2}}\right) \tag{51}$$

where $\hat{\boldsymbol{f}}_{i+\frac{1}{2}} = \hat{\boldsymbol{f}}(t, x_{i+\frac{1}{2}})$ are numerical fluxes defined through a reconstruction based on the information at the *stencil* points $S = \{x_{i-m}, \ldots, x_{i+n}\}$ such that

$$\hat{\boldsymbol{f}}_{i+1/2} = \hat{\boldsymbol{f}}(\boldsymbol{q}_{i-m}, \ldots, \boldsymbol{q}_{i+n}). \tag{52}$$

It is required that $\hat{\boldsymbol{f}}$ be Lipschitz continuous in all arguments and be consistent with the physical flux $\boldsymbol{f}$, i.e. that $\hat{\boldsymbol{f}}(\boldsymbol{q}, \ldots, \boldsymbol{q}) = \boldsymbol{f}(\boldsymbol{q})$, in order to guarantee that the solution converges to the weak solution of (38).

The numerical fluxes $\hat{\boldsymbol{f}}_{i+1/2}$ and $\hat{\boldsymbol{f}}_{i-1/2}$ arise respectively from the *upstream* and *downstream* contributions of a central scheme and they must follow a number of guidelines. To guarantee entropy dissipation, the flux is first split globally into positive and negative parts using Lax Friedrichs splitting as $\boldsymbol{f}(\boldsymbol{q}) = \boldsymbol{f}^+(\boldsymbol{q}) + \boldsymbol{f}^-(\boldsymbol{q})$, with

$$\boldsymbol{f}^{\pm}(\boldsymbol{q}) = \frac{1}{2}(\boldsymbol{f}(\boldsymbol{q}) \pm \alpha \boldsymbol{q}), \quad \text{with} \quad \alpha = \max\left(\frac{\partial \boldsymbol{f}(\boldsymbol{q})}{\partial \boldsymbol{q}}\right). \tag{53}$$

Here, under the consideration of *progressive waves*, it is assumed that $\partial \boldsymbol{f}(\boldsymbol{q})/\partial \boldsymbol{q} = c_0 + \beta \frac{|p_a|}{\rho_0 c_0}$. The reconstruction is then applied to each positive and negative fluxes separately before adding them up to give the final numerical flux.

Under the consideration of smooth data, a finite difference reconstruction of the flux, for instance $\hat{\boldsymbol{f}}_{i+\frac{1}{2}}^+$, can be formulated using $(2r-1)$ grid values distributed on a single large stencil,

$$S = \{x_{i-r+1}, \ldots, x_{i+r-1}\}, \quad r = 2, 3, \ldots, \tag{54}$$

as

$$\hat{\boldsymbol{f}}_{i+\frac{1}{2}}^+ = \sum_{l=-r+1}^{r-1} c_l \boldsymbol{f}^+(\boldsymbol{q}_{i+l}), \tag{55}$$

which yields a $(2r-1)$th-order approximation of the exact *upstream flux*, $\hat{\boldsymbol{f}}^+(q_{i+\frac{1}{2}})$. If smooth data cannot be guaranteed, it is convenient to consider the computation of a finite difference reconstruction of the flux, for instance $\hat{\boldsymbol{f}}_{i+\frac{1}{2}}^+$, using the solutions in r different sub-stencils,

$$S_k = \{x_{i+k-r+1}, x_{i+k-r+2}, \ldots, x_{i+k}\}, \quad k = 0, \ldots, r-1 \tag{56}$$

as

$$\hat{\boldsymbol{f}}_{i+\frac{1}{2}}^{+(k)} = \sum_{l=0}^{r-1} a_{k,l}^r \boldsymbol{f}_k^+(\boldsymbol{q}_{i+k-r+l}). \tag{57}$$

The constant coefficients $a_{k,l}^r$ are chosen such that the approximate solution is formally accurate to the order r in regions in which the exact solution is sufficiently smooth. The coefficients for cases $r = 2$ and $r = 3$ are found in table I of [26]. The numerical flux approximations on the small stencils in Eq. (57), can be seen as a convex combination of the numerical flux of Eq. (55), namely

$$\hat{\boldsymbol{f}}_{i+\frac{1}{2}}^+ = \sum_{k=0}^{r-1} \mathcal{C}_k \hat{\boldsymbol{f}}_{i+\frac{1}{2}}^{+(k)}. \tag{58}$$

Eq. (58) holds true, if in stencil, the solution is sufficiently smooth. Here, $\mathcal{C}_k$ are constant coefficients found in table II of [26]. On the other hand, if the solution or one of j-derivatives, $j \leq r$, contains a discontinuity, that stencil must be excluded from the flux approximation. This nonlinear procedure is referred to as an essentially non-oscillatory scheme. This is achievable by substituting $\mathcal{C}_k$ by nonlinear weights $\mathcal{W}_k$ and consider a convex combination of all the computed fluxes $\hat{\boldsymbol{f}}_{i+\frac{1}{2}}^{+(k)}$ in r sub-stencils as

$$\hat{\boldsymbol{f}}_{i+\frac{1}{2}}^+ = \sum_{k=0}^{r-1} \mathcal{W}_k \hat{\boldsymbol{f}}_{i+\frac{1}{2}}^{+(k)}, \tag{59}$$

where $\mathcal{W}_k$ is chosen such that the approximation recovers the $(2r-1)$-th order of accuracy in cases where the solution is sufficiently smooth. Explicit expression for $\mathcal{W}_k$ based on local smoothness indicators for orders $r = 2$ and $r = 3$ are given in [26].

The computation of negatively split flux, $\hat{\boldsymbol{f}}_{i+\frac{1}{2}}^-$, follows the same procedure of its positive counterpart. However the formulation must be made mirror symmetric with respect to $x_{i+1/2}$. Having the contributions from both, negative and positive split fluxes, the numerical flux at the interface $x_{i+1/2}$ is then simply obtained as

$$\hat{\boldsymbol{f}}_{i+\frac{1}{2}} = \hat{\boldsymbol{f}}_{i+\frac{1}{2}}^+ + \hat{\boldsymbol{f}}_{i+\frac{1}{2}}^-. \tag{60}$$

In this work, we have implemented the reconstructions for $r = 3$ and $r = 4$, namely the fifth- and seventh-order WENO reconstructions to deal with strongly nonlinear or discontinuous propagations. For simplicity, we will associate the fifth-order
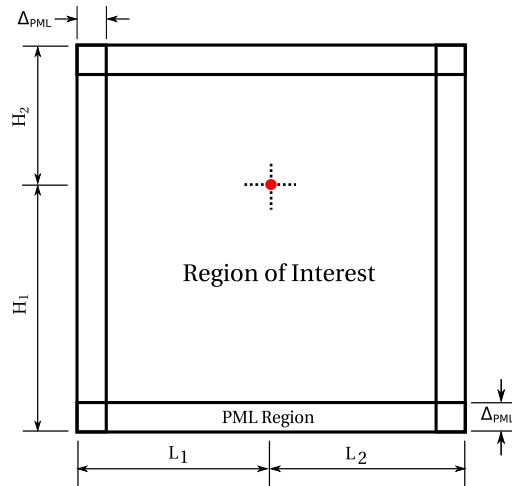
Fig. 3. Two-dimensional model. The red dot indicates the origin on the reference frame. (For interpretation of the references to color in this figure legend, the reader is referred to the web version of this article.)

WENO with the RK3 time integration scheme and refer to it as WENO5 scheme. Similarly, the seventh order will be associated with RK4(5), that will be referred as WENO7 scheme hereafter. Moreover, if the propagations are weakly nonlinear, we also consider pure polynomial reconstructions (in the sense of Eq. (55)) of fifth- and seventh-order. In a similar manner, they have respective association with RK3 and RK4(5) time integration schemes and they are respectively referred as FD5 and FD7 schemes. The details for the polynomial reconstruction are summarized in Appendix G. For the implementation details of the fifth- and seventh-order WENO reconstructions, we simply refer to [26] and [27], respectively.

Remark. In systems of conservation laws, such as the Euler equations, the WENO reconstruction is traditionally applied to the fluxes in the eigenvector space. Here, it is applied directly to the conserved quantities. This is done in order to obtain a simpler and explicit numerical implementation of the model to be solved in GPU accelerator. Although this strategy can lead to introducing some numerical dissipation, this can be compensated by requiring a finer grid with narrower space between nodes, Δx. Evidently, this strategy will increase the size and computational cost in our scheme. We consider it is an affordable price to pay when computing for one- and two-dimensional problems, provided that current GPU accelerator units can achieve hundreds of GigaFLOPS (10^9 floating-point operations per second).

4.1.6. Stability condition

The stability of any explicit finite-difference scheme proposed in Eq. (38) is governed by the Courant–Friedrichs–Levy (CFL) condition, i.e., the time step must be such that

$$\Delta t \leq \text{CFL} \frac{\Delta x}{s_{max}} \tag{61}$$

where s_{max} denotes the speed of the fastest intercell wave at the time step $t = n\Delta t$, $n = 0, 1, \ldots$; and CFL is the Courant number ($0 < \text{CFL} \leq 1$). In practice, the CFL condition is determined empirically. In addition, we obtain a reliable estimate of the largest intercell wave from

$$s_{max} = \max_{1 \leqslant i \leqslant N_x} \left(c_0 + \beta \frac{|\{p_a\}_i|}{\rho_0 c_0} \right), \tag{62}$$

where $\{p_a\}_i$ denotes the discrete value of the acoustic pressure field associated with an i-node.

4.2. Two-dimensional formulations

4.2.1. Cartesian formulation

Similarly, to solve for the nonlinear acoustic system in a two-dimensional Cartesian domain, as depicted in Fig. 3; we start by considering a two dimensional IVP of the form

$$\begin{cases} \text{PDEs:} & \boldsymbol{q}_t + \boldsymbol{f}(\boldsymbol{q})_x + \boldsymbol{g}(\boldsymbol{q})_y = 0, & (x, y) \in \Omega \in [L_1, L_2] \times [H_1, H_2], \, t > 0, \\ \text{ICs:} & \boldsymbol{q}(x, y, 0) = \boldsymbol{q}^{(0)}(x, y), & (x, y) \in \Omega, \\ \text{BCs:} & \boldsymbol{q}(x, y, t) = \boldsymbol{0}, & (x, y) \in \delta\Omega, \, t > 0, \end{cases} \tag{63}$$

where

$$\boldsymbol{q} = \begin{bmatrix} u_a \\ v_a \\ p_a \end{bmatrix} = \begin{bmatrix} q^{(1)} \\ q^{(2)} \\ q^{(3)} \end{bmatrix}, \qquad \boldsymbol{f}(\boldsymbol{q}) = \begin{bmatrix} q^{(3)}/\rho_0 \\ 0 \\ k_a q^{(1)} \end{bmatrix}, \qquad \boldsymbol{g}(\boldsymbol{q}) = \begin{bmatrix} 0 \\ q^{(3)}/\rho_0 \\ k_a q^{(2)} \end{bmatrix}. \tag{64}$$

In (64) $k_a = c_0^2 \rho_0 + \beta q^{(3)}$. For free-flow conditions near the boundaries, it is required to surround the computational domain by a non-zero width layers in which the incident waves should decay. Let us remark that those layers must also produce as weak as possible reflections at the interface of the *region of interest*. As depicted in Fig. 3, four PML layers are considered. Notice that in the corners of the domains, these layers may overlap each other. As before, perfectly matching layers (PMLs) developed on the basis of *complex coordinate stretching* [28] approach are considered to formulate the governing PDEs used inside these layers.

The nonlinear nature of the flux functions $\boldsymbol{f}(\boldsymbol{q})$ and $\boldsymbol{g}(\boldsymbol{q})$ make this coordinate transformation more involving. However, based on the numerical experience of the 1-d PML and given the fact that the linear acoustic model dominates the propagation speed of its nonlinear counterpart, it is safe to assume that $\boldsymbol{f}(\boldsymbol{q})$ and $\boldsymbol{g}(\boldsymbol{q})$ behave largely as linear functions. Therefore, the *complex coordinate stretching* method yields the augmented system

$$\begin{cases} \boldsymbol{q}_t + \tilde{\boldsymbol{f}}(\boldsymbol{q}, \boldsymbol{q}^{\{1\}})_x + \tilde{\boldsymbol{g}}(\boldsymbol{q}, \boldsymbol{q}^{\{1\}})_y = \mathcal{S}^{\partial\Omega}(\boldsymbol{q}, \boldsymbol{q}^{\{1\}}), \\ \boldsymbol{q}_t^{\{1\}} = \boldsymbol{q}, \end{cases} \tag{65}$$

where $\boldsymbol{q} = \{u_a, v_a, p_a\}^T$ is the vector of conserved quantities and $\boldsymbol{q}^{\{1\}} = \{u_a^{\{1\}}, v_a^{\{1\}}, p_a^{\{1\}}\}^T$ are the auxiliary function variables. $\tilde{\boldsymbol{f}}$ and $\tilde{\boldsymbol{g}}$ are the augmented flux functions defined as

$$\tilde{\boldsymbol{f}}(\boldsymbol{q}, \boldsymbol{q}^{\{1\}}) = \begin{bmatrix} p_a/\rho_0 \\ 0 \\ k_a(u_a + \sigma_y u_a^{\{1\}}) \end{bmatrix}, \qquad \tilde{\boldsymbol{g}}(\boldsymbol{q}, \boldsymbol{q}^{\{1\}}) = \begin{bmatrix} 0 \\ p_a/\rho_0 \\ k_a(v_a + \sigma_x v_a^{\{1\}}) \end{bmatrix},$$

where σ_x and σ_y are absorption coefficients defined in Appendix C and $\mathcal{S}^{\partial\Omega}$ is a source column vector that contains the absorption source terms, namely

$$S^{\partial\Omega}(\boldsymbol{q}, \boldsymbol{q}^{\{1\}}) = \begin{bmatrix} -\sigma_x u_a \\ -\sigma_y v_a \\ -(\sigma_x + \sigma_y)p_a + \sigma_x \sigma_y p_a^{(1)} \end{bmatrix}. \tag{66}$$

The formulation in system (65) corresponds to an unsplit-field formulation. Although it adds more complexity in the implementation and viscous memory requirements (as we are required auxiliary fields $\boldsymbol{q}^{\{1\}}$ to be stored). Our numerical experience shows that this formulation can avoid the reflections of acoustics propagations generated with the nonlinear model ($\beta \neq 0$), provided that the evolution proceeds with small time steps. Moreover, it is found that the corrections of the acoustic velocities inside the flux functions can be safely neglected. Therefore, the governing model considered in the 2-d PML regions is

$$\text{PML-2d} \begin{cases} \dfrac{\partial u_a}{\partial t} + \dfrac{1}{\rho_0}\dfrac{\partial p_a}{\partial x} = -\sigma_x u_a, \\ \dfrac{\partial v_a}{\partial t} + \dfrac{1}{\rho_0}\dfrac{\partial p_a}{\partial y} = -\sigma_y v_a, \\ \dfrac{\partial p_a}{\partial t} + \dfrac{\partial(k_a u_a)}{\partial x} + \dfrac{\partial(k_a v_a)}{\partial y} = -(\sigma_x + \sigma_y)p_a + \sigma_x \sigma_y p_a^{(1)}, \\ \dfrac{\partial p_a^{(1)}}{\partial t} = p_a, \end{cases} \tag{67}$$

where $p_a^{\{1\}}$ is the only auxiliary field to be appended to the nonlinear acoustic system. Unlike the vector field, the pressure field cannot be split into its Cartesian components and therefore the extra field $p_a^{\{1\}}$ arises as consequence of the unsplit condition.

Remark. Strictly speaking the 2-d PML formulation in Eq. (67) is not perfect, as in this formulation the corrections for the velocity fields have been neglected. However, by considering a slightly thicker PML layer, it is possible to effectively reduce the reflection to almost zero of any incoming wave with high amplitude. In this work, excellent results with PML layers of 20 nodes have been obtained.

4.2.2. Axisymmetric formulation

The formulation of a two-dimensional axisymmetric NAS model is obtained by introducing the definitions of gradient and divergence in polar coordinates, namely

$$\begin{cases} \nabla f = \frac{\partial f}{\partial r}\hat{\mathbf{r}} + \frac{\partial f}{\partial z}\hat{\mathbf{z}}, \\ \nabla \cdot \boldsymbol{\upsilon} = \frac{1}{r}\frac{\partial r\upsilon_r}{\partial r} + \frac{\partial \upsilon_z}{\partial z}, \end{cases} \tag{68}$$

into Eq. (63). In vector notation, the resulting axisymmetric formulation of the NAS equations simply reads

$$\text{2-d Axisymmetric:} \begin{cases} \boldsymbol{q}_t + \boldsymbol{f}(\boldsymbol{q})_r + \boldsymbol{g}(\boldsymbol{q})_z = -\frac{k_a q^{(1)}}{r}\mathbf{e}_3, \end{cases} \tag{69}$$

where $\boldsymbol{q}$, $\boldsymbol{f}(\boldsymbol{q})$, $\boldsymbol{g}(\boldsymbol{q})$ are defined as in relations (64) and $\mathbf{e}_3$ represents a constant column vector with zero elements, except for a unit element in the third row.

4.2.3. Formulation with forcing term

In analogy to the formulation in section 4.1.3, introducing a harmonic signal in the two-dimensional region of interest is achieved by considering a forcing source term in the mass equation. So that the governing system of equations becomes

$$\text{NAS-2d+F:} \begin{cases} \boldsymbol{q}_t + \boldsymbol{f}(\boldsymbol{q})_x + \boldsymbol{g}(\boldsymbol{q})_y = P_0\frac{c_0^2}{\omega}\exp{(+i\omega t)}\delta_{\Delta x}(x_i - x^*)\delta_{\Delta y}(y_j - y^*)\mathbf{e}_3, \end{cases} \tag{70}$$

where $\mathbf{e}_3 = \{0, 0, 1\}^T$ is a unit vector that ensures that the forcing term is only applied in the equation of mass. $\delta(x)$ and $\delta(y)$ are Dirac delta functions and both have m^{-1} units. (x^*,y^*) are the Cartesian coordinates of the point source and they may or may not coincide with a discrete point in the domain. P_0 is the amplitude of the signal given in MPa and ω is the angular frequency of the harmonics signal given in rad/s. Notice that transforming back the nonlinear term to a time derivative form and partially deriving the momentum and mass equation with respect to space and time, respectively. The system is found to be consistent with the forced version of Westervelt equation, namely

$$\frac{\partial^2 p_a}{\partial x^2} + \frac{\partial^2 p_a}{\partial y^2} - \frac{1}{c_0^2}\frac{\partial p_a}{\partial t} = -\frac{\beta}{\rho_0 c_0^4}\frac{\partial^2 p_a^2}{\partial t^2} - i\, P_0 \exp{(+i\omega t)}\delta(x - x^*)\delta(y - y^*). \tag{71}$$

The discretization of each of the delta functions is considered as indicated in Eq. (47), so that the product $\delta(x)\delta(y)$ is simply performed as a tensor product of the discrete Dirac delta functions $\delta_{\Delta x}(x)\delta_{\Delta y}(y)$.

4.2.4. Temporal and spatial discretization

The two-dimensional NAS formulations in Eqs. (67), (69) and (70) can all be expressed in a semi-discrete form as

$$\frac{\partial \boldsymbol{q}}{\partial t} = -\boldsymbol{f}(\boldsymbol{q})_x - \boldsymbol{g}(\boldsymbol{q})_y + \mathcal{S}(\boldsymbol{q}, x, y, t) = \text{L}(\boldsymbol{q}), \tag{72}$$

where L$(\boldsymbol{q})$ represents the contribution of all convective operators and source terms. In this form the temporal evolution of the conserved quantities $\boldsymbol{q}$ can be explicitly performed using either a RK3 or a RK4(5) scheme as presented in section 4.1.4.

For multiple dimensional problems, the finite difference WENO scheme is performed in a dimension by dimension fashion, with the one-dimensional procedure discussed in subsection 4.1.5, and used in each dimension. In other words, the convective operators $\boldsymbol{f}(\boldsymbol{q})_x$ and $\boldsymbol{g}(\boldsymbol{q})_y$ can be simply discretized as

$$\text{L}(\boldsymbol{q}_{ij}) = -\frac{\hat{\boldsymbol{f}}_{i+\frac{1}{2},j} - \hat{\boldsymbol{f}}_{i-\frac{1}{2},j}}{\Delta x} - \frac{\hat{\boldsymbol{g}}_{i,j+\frac{1}{2}} - \hat{\boldsymbol{g}}_{i,j-\frac{1}{2}}}{\Delta y} + S(\boldsymbol{q}_{ij}) \tag{73}$$

where the numerical flux $\hat{\boldsymbol{f}}_{i+1/2,j}$ can be computed from $\boldsymbol{q}_{ij}$ with fixed j, exactly the same way as in the one dimensional case. Likewise for $\hat{\boldsymbol{g}}_{i+1/2,j}$. The computational cost is exactly the same as that spent in the one-dimensional case per point direction.

Lastly, as in the one dimensional case, the stability of such scheme is also governed by the CFL condition, so that time step must satisfy

$$\Delta t = \frac{\text{CFL}}{s_{max}}\frac{1}{\frac{1}{\Delta x} + \frac{1}{\Delta y}} \tag{74}$$

where s_{max} is defined in Eq. (62) and denotes the speed of the fastest intercell wave at time $t = n\Delta t$, $n = 0, 1, \ldots$; and CFL $\in [0, 1[$ is the Courant number.

4.3. Extension to thermoviscous models

In previous subsections we have concentrated on the numerical implementation of the nonlinear acoustic system of equations. Here, the extension to include dissipative and local nonlinear effects is presented. Let us consider a one-dimensional formulation of the conservative thermoviscous system (21) cast in vector notation

$$\boldsymbol{q}_t + \boldsymbol{f}(\boldsymbol{q})_x = \bar{\mathcal{D}}\,\nabla^2\boldsymbol{q} + S(\boldsymbol{q}, x, t) \tag{75}$$

where q, $\boldsymbol{f}\boldsymbol{q}$ and $\boldsymbol{g}(\boldsymbol{q})$ are defined as in Eq. (25), $\bar{\mathcal{D}}$ is a diagonal matrix whose components are defined in terms of the physical properties of the domain, namely $\bar{\mathcal{D}}_{11} = \frac{1}{\rho_0}(\mu_B + \frac{4}{3}\mu)$ and $\bar{\mathcal{D}}_{22} = \frac{\kappa}{\rho_0}(\frac{1}{c_v} - \frac{1}{c_p})$, and $S(\boldsymbol{q}, x, t)$ is a general representation of the contributions of source terms such as the absorbing terms for PML layers and the Lagrangian rates of change. Here $\bar{\mathcal{D}}_{11}$ and $\bar{\mathcal{D}}_{22}$ variables can take values in $[0, \infty[$. It is evident that Eq. (75) is a balance law, where the diffusive operator plays a decisive role in the solution strategy. If the contribution of the diffusive operator is small, a fully explicit implementation of Eq. (75) might be suffice to describe the acoustic propagation in thermoviscous media. However, if the contribution of the diffusive operator dominates the nonlinear convective contribution, we then propose an *asymptotic-preserving* numerical scheme to solve for the conservative thermoviscous formulation introduced in this work. For our solver expressed in semi-discrete form, we obtain

$$\frac{\partial \boldsymbol{q}(t)}{\partial t} = -\underbrace{\boldsymbol{f}(\boldsymbol{q})_x + S(\boldsymbol{q}, x, t)}_{explicit} + \underbrace{\bar{\mathcal{D}}\,\nabla^2\boldsymbol{q}}_{implicit} = \mathrm{L}^E(\boldsymbol{q}) + \bar{\mathcal{D}}\,\nabla^2\boldsymbol{q}, \tag{76}$$

where $\mathrm{L}^E(\boldsymbol{q})$ denotes the contribution of all operators treated in an explicit fashion, as introduced in section 4.1. Notice that we only choose to solve the diffusive operator implicitly.

Let us concentrate on a single component $q^{(l)}$, $l = 1, 2$; of the vector of conserved quantities, $\boldsymbol{q}$. For clarity, the upper index (l) is omitted hereafter. A 1st-order time-marching scheme of a single l-component takes the form

$$\frac{\{q\}_i^{n+1} - \{q\}_i^n}{\Delta t} = \{\mathrm{L}^E\}_i^n + \bar{\mathcal{D}}_{ll}\, D\,\{q\}_i^{n+1}, \tag{77}$$

where D represents a positive definite operator obtained using a standard centered difference stencil. By solving explicitly the values of $\{q\}_i^{n+1}$ we obtain the following scheme

$$\{q\}_i^{n+1} = (I - \Delta t\,\bar{\mathcal{D}}_{ll}\, D)^{-1}[\{q\}_i^n + \Delta t\,\{\mathrm{L}^E\}_i^n]. \tag{78}$$

Let us remark that although we solve for the contribution of diffusive term implicitly, a fully explicit numerical scheme can be derived. The advantage of this formulation becomes more evident if the coefficients of $\bar{\mathcal{D}}$ were to be considered as function of space. In heterogeneous media, it is desirable that in the regions where the scheme approaches the inviscid conditions, $\bar{\mathcal{D}} \to 0$, the scheme automatically approaches

$$\boldsymbol{q}^{n+1} = \boldsymbol{q}^n + \Delta t\,\mathrm{L}^E(\boldsymbol{q}^n), \tag{79}$$

which corresponds to the 1st-order explicit time-marching scheme of the NAS equations. In other words, the numerical scheme preserves the NAS equations as the inviscid asymptotic limit of the conservative thermoviscous system of equations. Higher-order time-marching schemes can be obtained by means of the implicit-explicit Runge–Kutta schemes. These schemes and their implementation have been already explored by one of the authors in the context of kinetic theory using Flux Reconstruction [29] and WENO [30] methods in multiple dimensions. However, results using high-order schemes for the acoustic system will be reported elsewhere.

5. Numerical tests

The following examples are all related to the numerical simulations of nonlinear acoustic propagations that result from a high intensity focused ultrasound (HIFU) test. This test can be performed as a two-dimensional problem with axial symmetry since the domain is assumed to be homogeneous. Here, the essential building blocks, namely a one- and two-dimensional Cartesian and axisymmetric formulation of the NAS equations, and extensions of this formulations were presented in § 4.

Here, we are initially interested in verifying that our implementation is consistent with linear expectations and it converges for nonlinear propagations with shocks. Then, the long-term physical expectation of the NAS equations in 1-d is investigated. Lastly, the numerical acoustic descriptions of a HIFU test are explored for propagations in linear, weakly nonlinear and strongly nonlinear regimes in homogeneous thermoviscous media. For simplicity, the shorthand notations of "LAS", "NAS" and "TAS" will be adopted in this section to refer to the linear acoustic system, the nonlinear acoustic system (22) and the thermoviscous acoustic system (21), respectively.
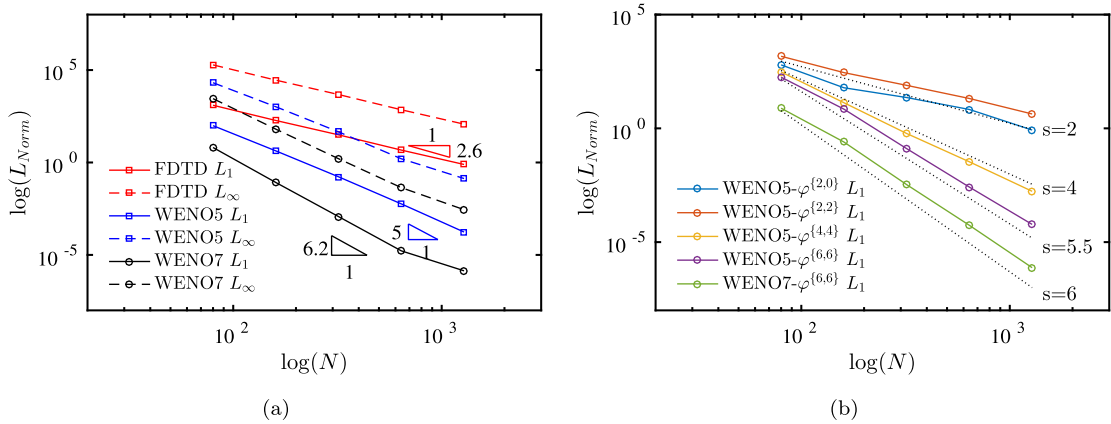
Fig. 4. Order of accuracy (OOA) obtained for NAS-WENO solvers using linear propagations. In (a), results for NAS initial value problem test in Cartesian domain. In (b), forced NAS test results using a discrete Dirac delta function based on different φ-grid functions. Moreover, the variable s denotes the slope of the dashed lines. More details are provided in text.

5.1. Initial value problems with the nonlinear acoustic system

As it has been shown in section 3.2, the *linear acoustic system* is the mechanism that dominates the propagation speed of its nonlinear counterpart. Thus, it is critical to ensure that its implementation achieves the expected accuracy and convergence rates before exploring the nature of the *nonlinear acoustic system*. Similarly, it is essential to ensure that the NAS model performs correctly before targeting any TAS model.

5.1.1. One-dimensional Cartesian propagations

Consider the IVP (38) in a physical domain for $x = [-1, 1]$ cm and $t > 0$ to be solved with an initial condition of the form

$$\boldsymbol{q}_0(x) : \begin{cases} u_a(x, 0) = 0, \\ p_a(x, 0) = g(x), \end{cases} \tag{80}$$

where $g(x) = P_0 \exp(-2E4\, x^2)$ in MPa is a smooth Gaussian profile with $P_0 = 10$ MPa of amplitude centered about the origin of the domain. The domain is homogeneous with $\rho_0 = 1000$ kg/m^3 and $c_0 = 1500$ m/s. Here, for the sake of completeness, PML boundaries were considered to emulate free-boundary flow conditions at both ends of the domain. The NAS model in the IVP (38) is then associated with the WENO5 scheme and is discretized in a uniform grid.

For $\beta = 0$, the NAS equations simply reduce to the LAS model. A convergence test is performed by evolving the IVP up to $t = 4$ µs by measuring the error of L_1 and L_∞ norms with respect to d'Alembert's exact solution for the wave equation problem. The problem is then solved using uniform grids with $N = 81, 161, 321, 641$, and 1281 nodes. The CFL condition was tuned for each case so that the error L_1 and L_∞ norms of the final outputs are recorded. For the sake of comparison, we also proceed in the same manner for our NAS-WENO7 and the Westervelt FDTD solver [31].

As the linear propagation model evolves, the initial Gaussian profile is split into two identical Gaussian profiles, each of half the original amplitude, and both are displacing in opposite directions of the domain. As expected, NAS model associated to a WENO reconstruction $r = 3$ converges at a rate of 5th-order, while the WENO reconstruction $r = 4$ without mapped nonlinear weight converges approximately at a rate of 6th-order [32]. In Fig. 4a, the order of accuracy (OOA) of each solver are summarized.

We now consider a nonlinear propagation with $\beta = 10$ [-].[1] For convenience, we extend the solution domain to $x = [-2.5, 2.5]$ cm and let our NAS-WENO5 solver evolve up to a final time of $t = 12$ µs under fix CFL condition of 0.10. The numerical solutions of the NAS-WENO5 are compared with those obtained with the Westervelt FDTD solver under the same parameters. It has been observed that if the solution for the nonlinear propagations is smooth, the agreement between the results of each solver is excellent so that they can be used for making a qualitative comparison. In Fig. 5a, the NAS-WENO5 and NAS-WENO7 solvers were used to evolve a weak-nonlinear propagation on a uniform grid with spacing $\Delta x = 1E{-}4$ m. The solution of the Westervelt FDTD solver on a uniform grid with $\Delta x = 0.1E{-}5$ m is then used as a reference solution for the nonlinear propagation and the linear propagation profile has been included to evidence the nonlinear deformation of the profile as it displaces. All solutions are in good agreement.

We consider a nonlinear propagation with $\beta = 100$ and proceed to solve again the IVP up to time $t = 12$ µs. In this case, the nonlinear accumulation is so fast that it gives rise to a shock profile. The NAS-WENO5 solver is evolved with uniform

---

[1] The nonlinear parameter $\beta = 1 + \frac{B}{2A}$ is dimensionless.
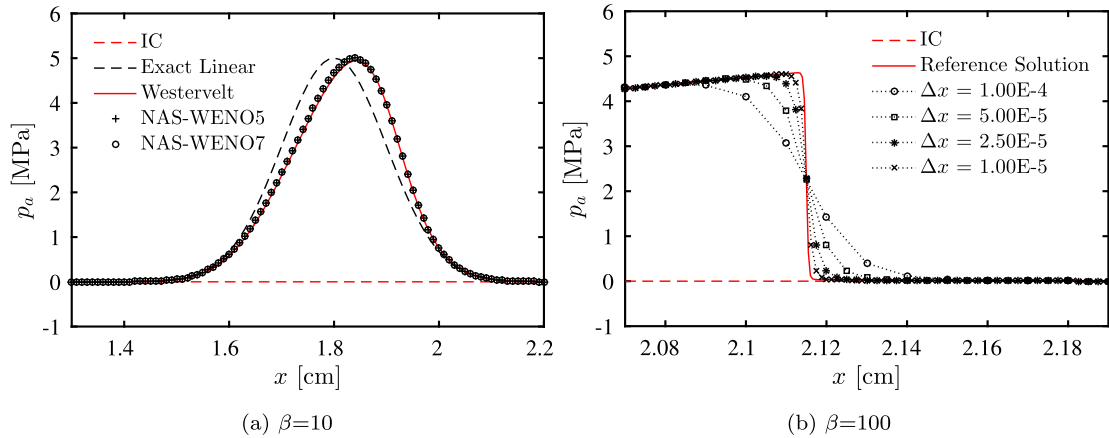
Fig. 5. Nonlinear propagations in a single spatial domain obtained by evolving the NAS equations, with a Gaussian profile as the initial condition, to time $t = 12$ μs. (a) Solution profile for the right running wave obtained with NAS-WENO5 and NAS-WENO7 solvers on a uniform grid with $\Delta x = 1E$-4 m. A Westervelt FDTD solution in a finer grid is used as a reference. In (b) a convergence test for a shock structure solution is performed with a NAS-WENO5 scheme for propagations with $\beta = 100$. A NAS-WENO7 solution in a refined grid is used as the reference solution. More details are given in the text.
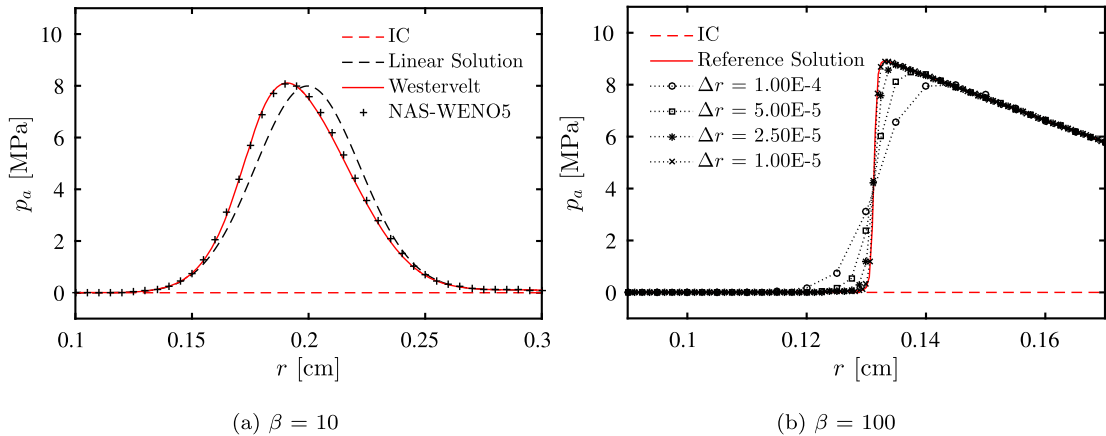
Fig. 6. Nonlinear wave propagations in a domain with axial symmetry obtained by evolving a NAS axisymmetric model, for a Gaussian profile as initial condition, to time $t = 2$ μs. (a) Solutions profiles for the left running profile solved using NAS-WENO5 solver in a uniform grid with $\Delta x = 5E$-5 m. A Westervelt FDTD solution in a finer grid is used as a reference. In (b) a convergence test for a developing shock profile is performed with a NAS-WENO5 scheme for propagations with $\beta = 100$. A NAS-WENO7 solution in a refined grid is used as the reference solution. More details are given in the text.

meshes $\Delta x = 1E$-4, 5E-5, 2.5E-5 and 1E-5 m. At this level, the Westervelt FDTD solver fails to resolve the shock profile and therefore is not reported. The results are put together in Fig. 5b. The solutions depict that the model is converging to the solution of the shock. Here the *reference solution* is built by running the NAS-WENO7 solver in a grid with a spacing of $\Delta x = 1E$-6 m. The results show that as the mesh is refined the method is converging to the discontinuous shock profile in the solution.

5.1.2. One-dimensional axisymmetric propagations

In section 4.1.2, it was shown that the IVP (38) can be formulated into an axisymmetric problem by introducing a correction source term, and solving in a radial domain for $r = [0, 1]$ cm for $t > 0$ μs. In this test, the initial condition in Eq. (80) is again considered. However, we now use a narrower Gaussian profile defined as $g(r) = P_0 \exp\left(-1E5 (r - 0.5)^2\right)$ MPa, where $P_0 = 10$ MPa is the amplitude of the Gaussian profile.

Notice that $g(r)$ is now centered about $r = 0.5$ cm of the spatial domain. Moreover, for the sake of completeness, PML boundaries were considered to emulate free-boundary flow conditions at the right-end of the domain, while a symmetric boundary condition is assumed at $r = 0$ cm.

In analogy to the Cartesian propagation tests, the propagation of a Gaussian profile under the nonlinear axisymmetric formulation is evolved up to time $t = 2$ μs, using $\beta = 10$ and $\beta = 100$. The solutions of both propagations are depicted in Figs. 6a and 6b, respectively.
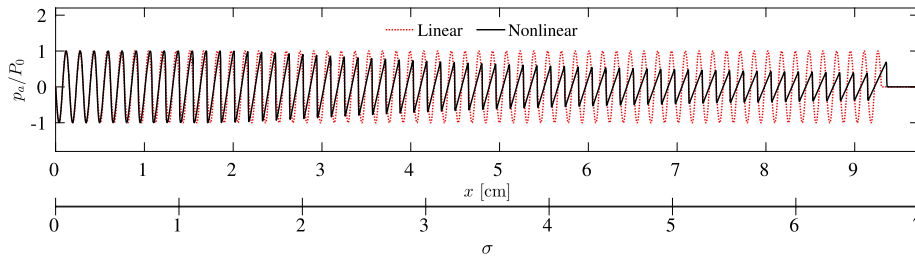
Fig. 7. Linear and nonlinear pressure profiles, obtained by respectively evolving a boundary value problem with LAS and NAS equations up to time $t = 60$ μs. Here a 5th-order WENO scheme associated with SSP-RK3 is used on a uniform grid with $\Delta x = 1E-5$ m. The solutions depict the departure of the nonlinear behavior from the linear approximation model for a long term propagation. More details are given in the text. (For interpretation of the references to color in this figure, the reader is referred to the web version of this article.)

To verify the axisymmetric NAS-WENO5 solution of a weakly nonlinear propagation, we compare out solution with the numerical solution obtained by an axisymmetric implementation of the Westervelt equation using a DFDT method under the same parameters. Namely

$$\frac{\partial^2 p_a}{\partial r^2} + \frac{1}{r}\frac{\partial p_a}{\partial r} + \frac{1}{c_0^2}\frac{\partial^2 p_a}{\partial t^2} = -\frac{\beta}{\rho_0 c_0^4}\frac{\partial^2 p_a^2}{\partial t^2}. \tag{81}$$

For the strongly nonlinear propagation, the *reference solution* is built by running the NAS-WENO7 solver in a grid with a spacing of $\Delta r = 1E-6$ m. The results are analogous to those obtained in their Cartesian counterparts.

5.2. Asymptotic verification of a forward propagating wave

Hamilton in [18, chap. 3.7] has shown that the Burgers' equation can be recovered for single-sided propagations of the Westervelt equation. In other words, the Westervelt model becomes the Burgers' model for a single-sided propagation. Given the similarities of the inviscid Westervelt model and the NAS model, it is expected that the NAS model can recover the inviscid Burgers' asymptotic behavior in a long term propagation. In this test, we aimed to justify this assumption numerically by studying the long term nonlinear propagation of a sinusoidal signal with the NAS model.

In this test, we consider a forced NAS formulation of the form

$$\begin{cases} \frac{\partial}{\partial t}(u_a) + \frac{\partial}{\partial x}(p_a/\rho_0) = 0, \\ \frac{\partial}{\partial t}(p_a) + \frac{\partial}{\partial x}(k_a u_a) = c_0 P_0 \sin(2\pi f\, t)\delta(x - x^*), \end{cases} \quad \text{for } x \in \Omega \in [a, b], t \geq 0, \tag{82}$$

with a homogeneous initial condition, namely

$$\begin{cases} u_a(x, 0) = 0, \\ p_a(x, 0) = 0. \end{cases} \tag{83}$$

In this NAS formulation, a sinusoidal signal of amplitude $2P_0$ (in Pa) and with frequency f (in Hz), is introduced at point $x^* \in [a, b]$. For this test we assume free-flow condition at the boundaries, therefore, PML absorbing ramps are set at both ends of the domain as depicted in Fig. 1. Notice that in the linear scenario, $\beta = 0$, the acoustic pressure field has an exact solution of the from

$$p_a = P_0 \sin(2\pi f(t - |x - x^*|/c_0)), \text{ for } x \in [a, b], t \geq 0. \tag{84}$$

We consider testing the order of accuracy (OOA) of the model using a linear propagation test ($\beta = 0$) and the knowledge of the exact solution in Eq. (84). Here a sinusoidal signal with $P_0 = 10$ MPa, and $f = 1$ MHz is considered to be evolved using the forced NAS solver discretized using both WENO5 and WENO6 schemes and using the discrete version of the $\delta(x)$ as proposed in Eq. (47). In this test, we study the discrete formulation of a Dirac delta function based on the grid functions $\varphi^{\{2,0\}}$, $\varphi^{\{2,2\}}$, $\varphi^{\{4,4\}}$ and $\varphi^{\{6,6\}}$ proposed in [23]. A homogeneous domain with $c_0 = 1500$ m/s and $\rho_0 = 1000$ kg/m^3 is considered. Moreover, the domain is assumed to be $\Omega \in [-1, 6]$ mm of length and to be discretized using 81, 161, 321, 641 and 1281 uniformly distributed nodes. For this test, the sinusoidal signal is assumed to be introduced at $x^* = 0$. Notice that x^* does not coincide with a discrete node on the numerical domain. For each of the proposed discrete domains, the system in Eq. (82) is evolved up to time $t = 4$ μs. For each case, the L_1-norm error is computed in the range of $x \in [0, 5]$ mm (the region of interest) and the CFL parameter is adjusted to obtain the minimum error that the formulation can achieve. The results then are reported in Fig. 4b and show that, for the linear scenario, the NAS discretization using WENO schemes associated with the discrete point sources manage to achieve optimal convergence rates.

We now consider the propagation of a sinusoidal signal with $f = 1$ MHz of frequency and $P_0 = 10$ MPa of amplitude on a homogeneous nonlinear domain with $\beta = 4.5$, $\rho_0 = 1055$ kg/m^3 and $c_0 = 1550$ m/s. The domain is assumed to be now
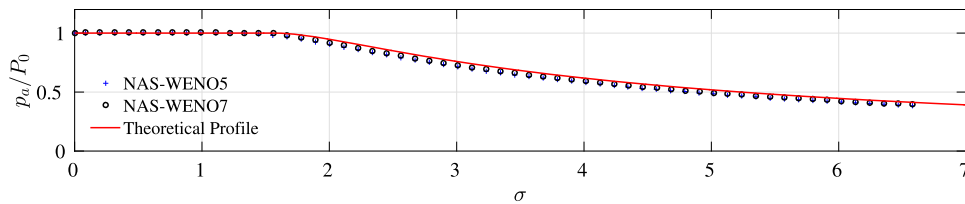
Fig. 8. Comparison of the pressure peak values with a theoretical expectation obtained from the Blackstock's analysis in [33]. In this result the single-sided propagation from the NAS equations is in good agreement with the inviscid Burgers' asymptotic behavior.

$\Omega \in [-0.1, 10]$ cm of length and the signal is assumed to be introduced at $x^* = 0$. The system is discretized on a uniform grid with $\Delta x = 1\text{E}{-}5$ m and will be evolved up to a final output time of $t = 60$ µs under a fixed CFL parameter of 0.5, initially using the WENO5 scheme. In Fig. 7, the full wave nonlinear propagation profile (in black) and its corresponding linear wave propagation (red dots line) were computed at same final output time. These results are then normalized with respect to P_0. From this result, it is evident that in the long term propagation, the wave patterns are different. Moreover, the *nonlinear cumulative effect* causes the shape of the sinusoidal wave to become steep and the wave is turned into a decaying sawtooth wave.[2]

To verify this solution, a theoretical expectation of the wave amplitude can be built from Blackstock's shock analysis, this is presented and summarized in Appendix D. In Fig. 8, the peaks of $|p_a/P_0|$ are compared to the theoretical expectation. This result shows that the numerical solution follows the expected trend predicted specially after the shock formation. However, the agreement between the expected values and the peaks is found to be of the order $O(\Delta x)$. We choose to re-run this case using the NAS-WENO7 scheme and plot the peaks of the resulting wave profile in Fig. 8 as well. Although the results with WENO7 show a significant improvement over those obtained with WENO5, the solution remains a first-order approximation. Although this result might not be so encouraging, it was expected, since WENO schemes can only guarantee high-order accuracy in smooth regions of the solution. Therefore, to inquire more on the quality of the results obtained in between of the shock structures, we choose to examine the time-domain profiles solutions at the specific x_σ-points of the domain.

5.2.1. Comparison to the inviscid burgers' classical solutions in time domain

To start this comparison, it is necessary to first introduce the σ-frame of reference. This frame of reference follows from the shock formation analysis of Blackstock, where $\sigma = 1$ characterizes the distance to the shock initial formation. Therefore σ-frame is related to the physical x-frame by the relation

$$\sigma = \frac{x}{\bar{x}}, \quad \text{where} \quad \bar{x} = \frac{c_0^3 \rho_0}{\beta P_0 \omega}. \tag{85}$$

Here $\bar{x}$ is the expected shock formation physical distance and is defined in terms of is the source amplitude, P_0, the source angular frequency, ω, the parameter of nonlinearity, β, the density and the sound speed of the media, ρ_0 and c_0 respectively.

For this test we choose to examine the points $\sigma \approx \{0.5, 0.99, \pi/2, 3, 4, 5\}$, so the NAS-WENO7 solver is re-run and save acoustic pressure data of points closest the chosen data points are collected. Under a fix CFL of 0.5 the time step is $\Delta t = 3.226$ µs. Because the time step is very tiny, the pressure data is collected every four time steps to build discrete time domain profiles. The "exact" time-domain profiles are then built using the classical solutions of the inviscid Burgers' equation summarized in Appendix E and evaluated at the discrete σ-distance of the chosen node. The comparison of the profiles is then reported in Fig. 9.

The results show that the discrete and the theoretical time-domain profiles are in excellent agreement, not only in the smooth region of the propagation but also in the region where the shocks are fully developed. The numerical results of this section are encouraging and provide evidence that the *nonlinear acoustic system* can provide excellent descriptions of finite amplitude propagations from weakly- to strongly-nonlinear propagation regimes with a simpler code and free of numerical artifacts. As a result it is encouraging to further explore the consequences of the NAS model beyond the one-dimensional cases.

5.3. High intensity focused ultrasound test

In this test, we are interested in solving the acoustic pressure field generated from a spherical surface cap (a bowl) acting as an acoustic pressure source. The scheme of the problem can be seen in Fig. 10. Here, the formulation in Eq. (21) is used as it considers the effects of diffraction, attenuation (diffusion) and nonlinear propagation. This configuration will be explored for linear, weakly nonlinear and strongly nonlinear propagation regimes.

---

[2] All this, is in accordance with the theoretical expectations, even for the unbalanced cycle at the head of the wave train which will decay at a rate of $\sigma^{-1/2}$, namely as N-wave [33].
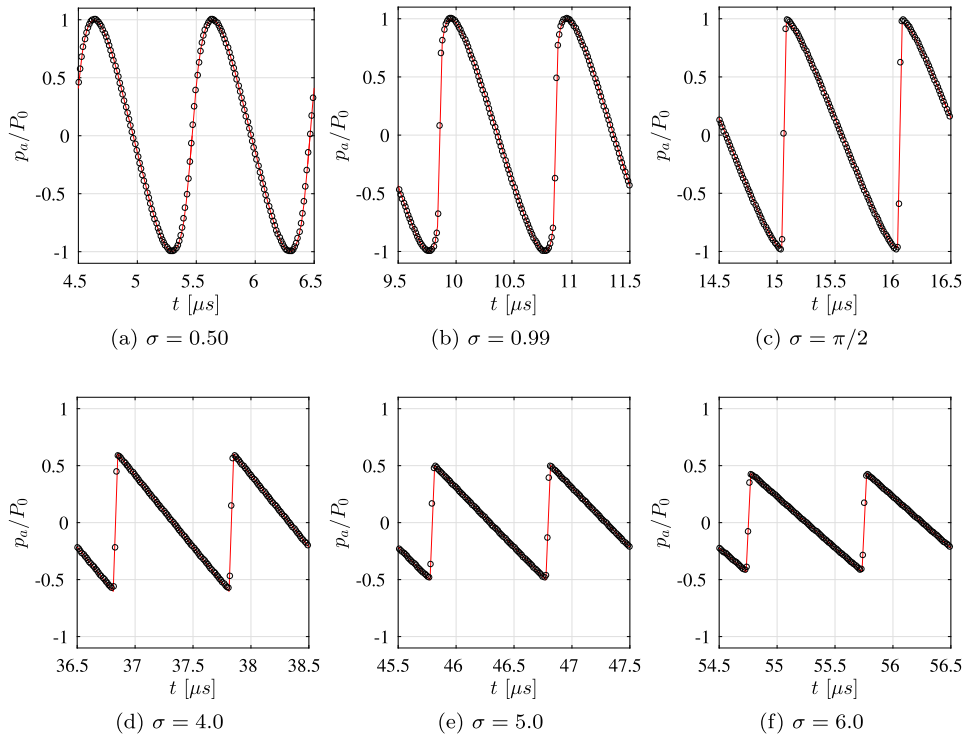
Fig. 9. Time-domain profiles obtained with NAS-WENO7 scheme (black circles) near spatial points that correspond to $\sigma = \{0.5, 0.99, \pi/2, 4, 5, 6\}$. Here the reference solutions (continuous red lines) for (a) and (b) are obtained with Fubini solution using 500 terms, (c) with Blackstock's solution using 200 terms and (d)–(f) are obtained with Fay inviscid solution using 5000 terms. The formulation details of the reference solutions are summarized in Appendix E. More details are provided in the text. (For interpretation of the references to color in this figure legend, the reader is referred to the web version of this article.)
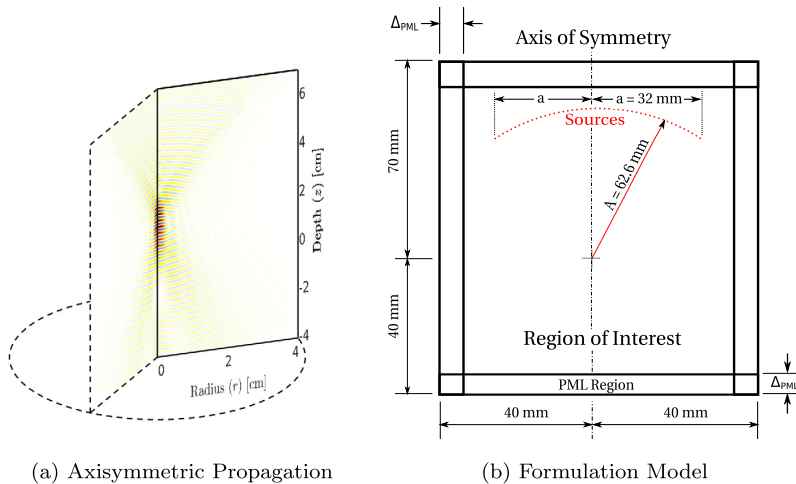
Fig. 10. Acoustic propagation in homogeneous media. In (a), given the homogeneity and the symmetry of the transducer, the problem is treated as 2-d problem with axial symmetry. In (b) the model formulation of PML layers and the *region of interest* is depicted.

5.3.1. Problem formulation and parameters

We are interested in modeling a focusing piston transducer typical for HIFU surgery with a radius of curvature of $A = 62.6$ mm, an aperture of $a = 32$ mm and introducing an acoustic signal at frequency $f = 1.06$ MHz. The media is considered as degassed water at 20° [C] so that it's assumed to have density of $\rho_0 = 1000$ kg/m^3, the speed of sound is $c_0 = 1500$ m/s and the attenuation loss coefficient is set to $\alpha = 0.026$ Np/m at 1 MHz.

To model the propagation of this focusing transducer, the governing system of equations to be solved inside the *region of interest* is assumed to be the axisymmetric formulation of the Eq. (21). For this case, however, the ratio $c_p/c_v \approx 1$ for
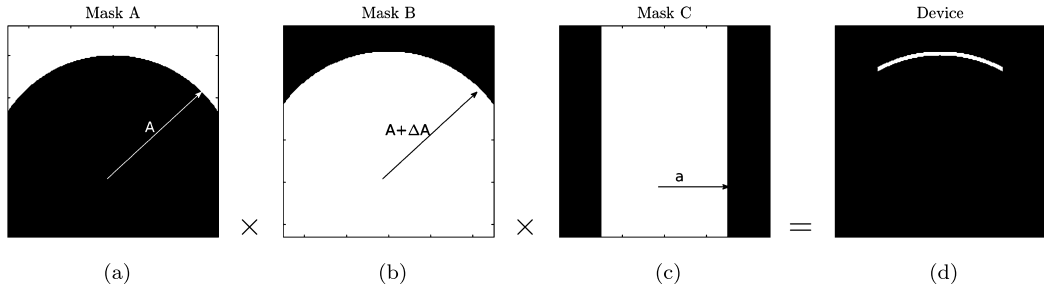
Fig. 11. In subfigures (a)–(c), three boolean arrays (or masks) are formulated in which the value of 1 (true) or 0 (false) is given to every cell in the discrete domain $\{\boldsymbol{x}\}_{ij}$. The white colored cells take the value of 1 while the black colored cells take the value of 0. The product of boolean arrays (a)–(c) is simply performed in a cell by cell fashion to build a boolean mask (d), referred in the text as $\{\mathbf{1}\}_{ij}^{device}$.

degassed water at room temperature. Therefore, the contribution of the diffusion coefficient in the pressure equation is neglected. The resulting system simply takes the form

$$
\text{TAS HIFU 2-d:} \quad
\begin{cases}
\frac{\partial u_a}{\partial t} + \frac{1}{\rho_0}\frac{\partial p_a}{\partial r} = \mathcal{D}\left(\frac{\partial^2 u_a}{\partial r^2} + \frac{\partial^2 u_a}{\partial z^2} + \frac{1}{r}\frac{\partial u_a}{\partial r} - \frac{u_a}{r^2}\right), \\
\frac{\partial v_a}{\partial t} + \frac{1}{\rho_0}\frac{\partial p_a}{\partial z} = \mathcal{D}\left(\frac{\partial^2 v_a}{\partial r^2} + \frac{\partial^2 v_a}{\partial z^2} + \frac{1}{r}\frac{\partial v_a}{\partial r}\right), \\
\frac{\partial p_a}{\partial t} + \frac{\partial (k_a u_a)}{\partial r} + \frac{\partial (k_a v_a)}{\partial z} = -\frac{k_a u_a}{r} + \mathrm{F},
\end{cases}
\tag{86}
$$

where $k_a = \rho_0 c_0^2 + \beta p_a$, and $\mathcal{D} = \frac{2c_0^3 \alpha}{\omega^2}$ is the diffusion coefficient due to attenuation of the media and $\mathrm{F} : \mathrm{F}(r, z, t)$ represents a forcing term that introduces a harmonic signal through an array of point sources as

$$
\mathrm{F}(r, z, t) = P_0 \frac{c_0^2}{\omega} \exp(i\omega t) \sum_{m=1}^{M} \delta(r - r_m^*)\,\delta(z - z_m^*),
\tag{87}
$$

where P_0 and ω are the amplitude and the angular frequency of the harmonic signal, respectively. The factor $\sum_{m=1}^{M} \delta(r - r_m^*)\,\delta(z - z_m^*)$ represents a scalar field that results from the superposition of m-point sources located at discrete spatial nodes in the numerical grid, $\{(r_m^*, z_m^*)\}$ where $m = 1, 2, \ldots, M$. Here, this list of discrete nodes is obtained by means a boolean mask $\{\mathbf{1}\}_{ij}^{device}$, as described in Fig. 11, so that the ij-indexes and their associated spatial coordinates are simply recovered for all the non-zero cells.

The numerical implementation of the convective terms is performed with high-order conservative finite-difference schemes as introduced in section 4.2.4. The diffusive terms are discretized using fourth-order finite-difference stencils. Lastly $\delta(r)$ and $\delta(z)$ are replaced by discrete approximations, namely $\delta_{\Delta r}(r_i)$ and $\delta_{\Delta z}(z_j)$, as introduced in sections 4.1.3 and 4.2.3. In this test, all the approximate Dirac delta functions are assumed to be based on the linear-hat grid function $\varphi^{\{2,0\}}$.

Let us remark that given the azimuthal symmetry of the problem, we only require to model half of the domain. This is true by simply requiring at the axis of symmetry that

$$
\left.\frac{\partial \boldsymbol{f}(\boldsymbol{q})}{\partial r}\right|_{r=0} = \mathbf{0}.
$$

Thus the computational domain only spans an area of 40 mm × 110 mm, and PML layers are considered at the top, bottom and right side of the domain. Here, for simplicity we will refer to the formulation in Eq. (86) as the TAS model for degassed water.

Lastly, to compare the numerical solutions of the present model with those obtained with other numerical solvers or exact solutions we make use of the definitions of positive and negative sound pressure distribution fields, namely

$$
p^+ = \max_{t \in T}(p_a) \quad \text{and} \quad p^- = \min_{t \in T}(p_a),
\tag{88}
$$

where $T = 1/f = 2\pi/\omega$ is the time of one period of the introduced sinusoidal signal.

5.3.2. Linear propagation verification

We start our verification study by considering linear inviscid propagation conditions in a homogeneous media. This is simply achieved by setting $\beta = 0$ and $\mathcal{D} = 0$ in (86) so that the TAS model for degassed water reduces to the LAS model inside the region of interest. For this case, an analytical solution is available in the form of the Rayleigh integral (O'Neil's classical solution in [34]) which provides an exact solution for the acoustic propagation along the axis of symmetry of the model.
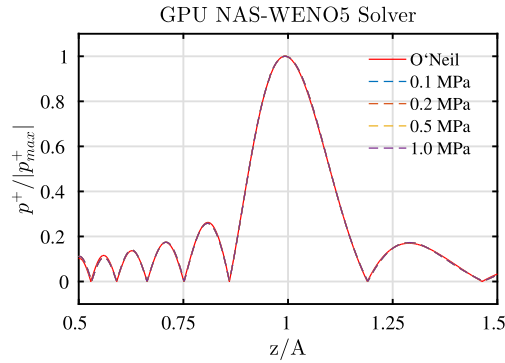
Fig. 12. Normalized pressure profiles on the axis of symmetry of the domain. These results are obtained by modeling linear acoustic propagation from a HIFU device: focal distance of $A = 62.6$ mm, aperture of $a = 32$ mm. Discrete solutions were obtained with the TAS-WENO5 solver and compared to O'Neil's exact solution of the Rayleigh Integral. The comparison of the normalized profiles showed a good agreement between the linear solutions, especially, near the focal plane ($z/A = 1$). More details are presented in the text.

The TAS-WENO5 scheme is initially chosen to evolve the linearized system. Given the length of the domain and the frequency of the source device, a uniform grid with $\Delta x = \Delta y = 2E\text{–}5$ m is considered. The spanned domain thus contains 2001×5501 nodes, for this grid 1,688 nodes are selected as point sources to represent half of the discrete profile of the focused device. To ensure the accuracy of the method, a fixed time step of $\Delta t = 2$ ns is considered. The system needs to be evolved up to time $t = 66$ μs, requiring 33,000 iterations. To perform this task, a CUDA-C implementation was developed, so that the problem can be run and solved on a Tesla K20c GPU unit. More details of the implementation are reported in Appendix A.

A focused device introducing a sinusoidal signal with $P_0 = 0.1$, 0.2, 0.5 and 1.0 MPa of amplitude is studied. The average computation time for the discrete models took about 6.45 hours. The solutions profiles are smooth, which indicate that perhaps the WENO reconstruction is too computationally demanding for this kind of the linear test. We re-run all cases using a fifth-order pure polynomial reconstruction. The same results are obtained but the computation time only required in average 2.2 hours. This is not surprising as the polynomial reconstruction performs well as it does not need to compute the WENO smooth measurements for every stencil evaluation.

The resulting p^+ profiles of the propagation at the axis of symmetry are obtained and normalized simply as $p^+/\max(p^+)$, and compared to the normalized profile obtained from the exact O'Neil solution. In Fig. 12, this comparison verifies that the linearized solutions scale linearly with respect to the amplitude of the input amplitude P_0 set on the device.

5.3.3. Weakly nonlinear verification

The TAS is now used to model acoustic propagations in homogeneous media with absorption and diffractions effects in weakly nonlinear regimes. For this test, the nonlinear parameter of degassed water is set to $\beta = 3.5$ and the diffusion coefficient takes the value of $\mathcal{D} = 1.562E\text{–}4$ m^2/s. Here the contribution of the diffusive terms due to $\mathcal{D}$ is very small, therefore an explicit discrete formulation of the diffusive operators is considered by means of fourth-order finite difference stencils.

To validate these results we compare to the solutions of the Westervelt model in axisymmetric coordinates [31], namely

$$\frac{\partial^2 p_a}{\partial r^2} + \frac{1}{r}\frac{\partial p_a}{\partial r} + \frac{\partial^2 p_a}{\partial z^2} - \frac{1}{c_0^2}\frac{\partial^2 p_a}{\partial t^2} = -\frac{\mathcal{D}}{c_0^4}\frac{\partial^3 p_a}{\partial t^3} - \frac{\beta}{\rho_0 c_0^4}\frac{\partial^2 p_a^2}{\partial t^2} - i\frac{\omega}{c_0^2}\text{F}. \tag{89}$$

The numerical solution of Eq. (89) was computed on the same grid and parameters assumed for NAS solver so that a direct comparison of solutions can be achieved.

In this validation, and ultrasound device with input sinusoidal signals of amplitude $P_0 = 0.05$, 0.1, 0.15, 0.2 0.25, 0.3 and 0.35 MPa are studied. In this test a uniform grid with $\Delta x = \Delta y = 2E\text{–}5$ m is considered. The spanned domain thus contains 2001×5501 nodes, for this grid 1,688 nodes are selected as point sources to represent half of the discrete profile of the focused device. To ensure the accuracy of the method, a fixed time step of $\Delta t = 2$ ns is considered. The system needs to be evolved up to time $t = 66$ μs, requiring 33,000 iterations. Because we only consider to obtain smooth solutions in the weak nonlinear propagations, the TAS solver associated with an FD5 reconstruction is used for all cases. The results were computed with a CUDA-C implementation that is run on a K20c Tesla GPU. The computation time took in average 2.3 hours.

The resulting p^+ and p^- profiles at the axis of symmetry are compared with their linear expectation. All results are smooth and for space we only report the cases of p_0: 0.1, 0.2 and 0.3 in Fig. 13. In Fig. 13 (a, c, e), the results verify that p^+ and $|p^-|$ are not symmetrical and the larger the amplitude of the propagation from the focused device, the greater the disagreement between the linear and nonlinear models. In Fig. 13 (b, d, f) the waveforms obtained at the final time $t = 66$ μs are compared for both solvers. The results indicate that the solutions of both numerical solvers are in a good agreement.
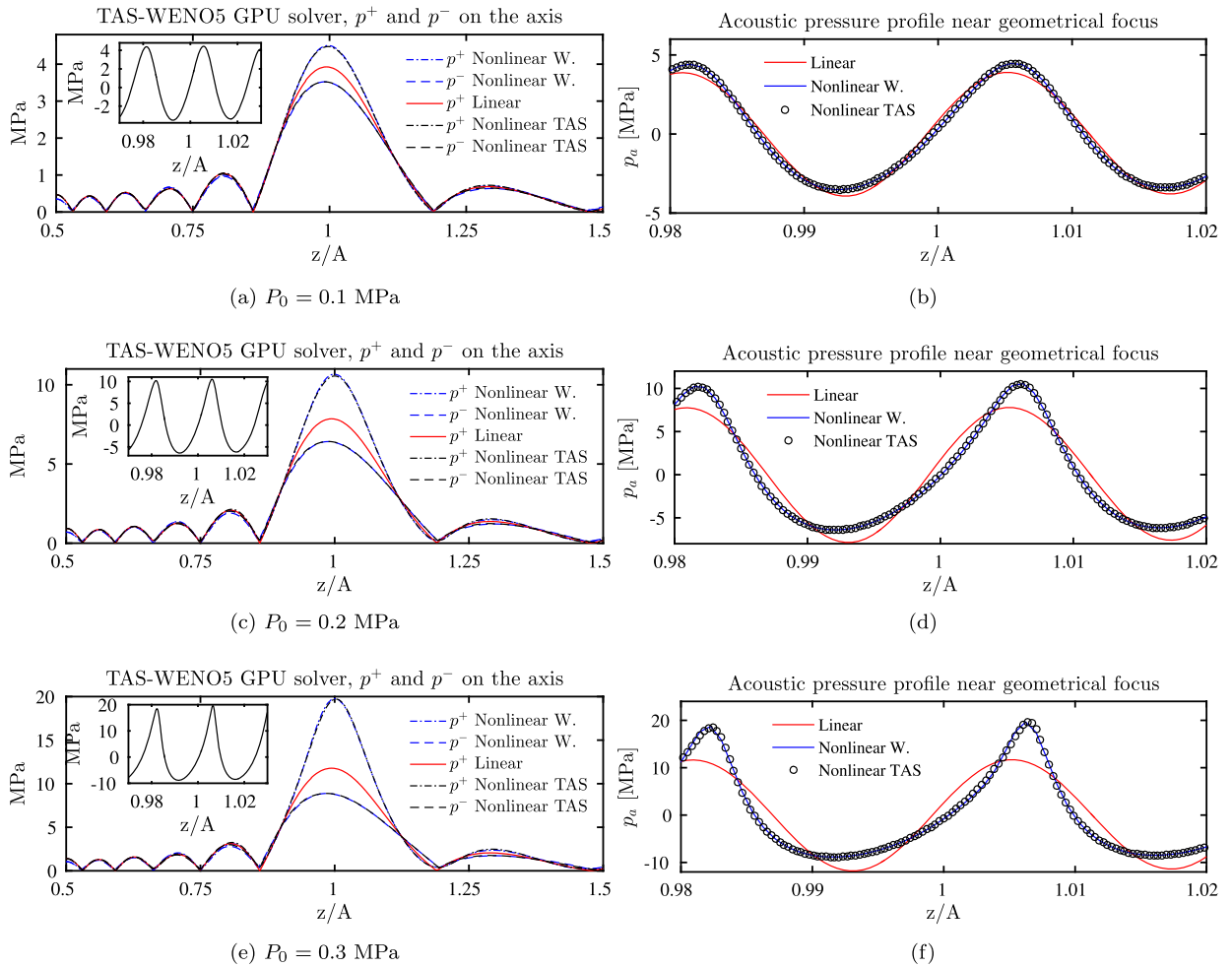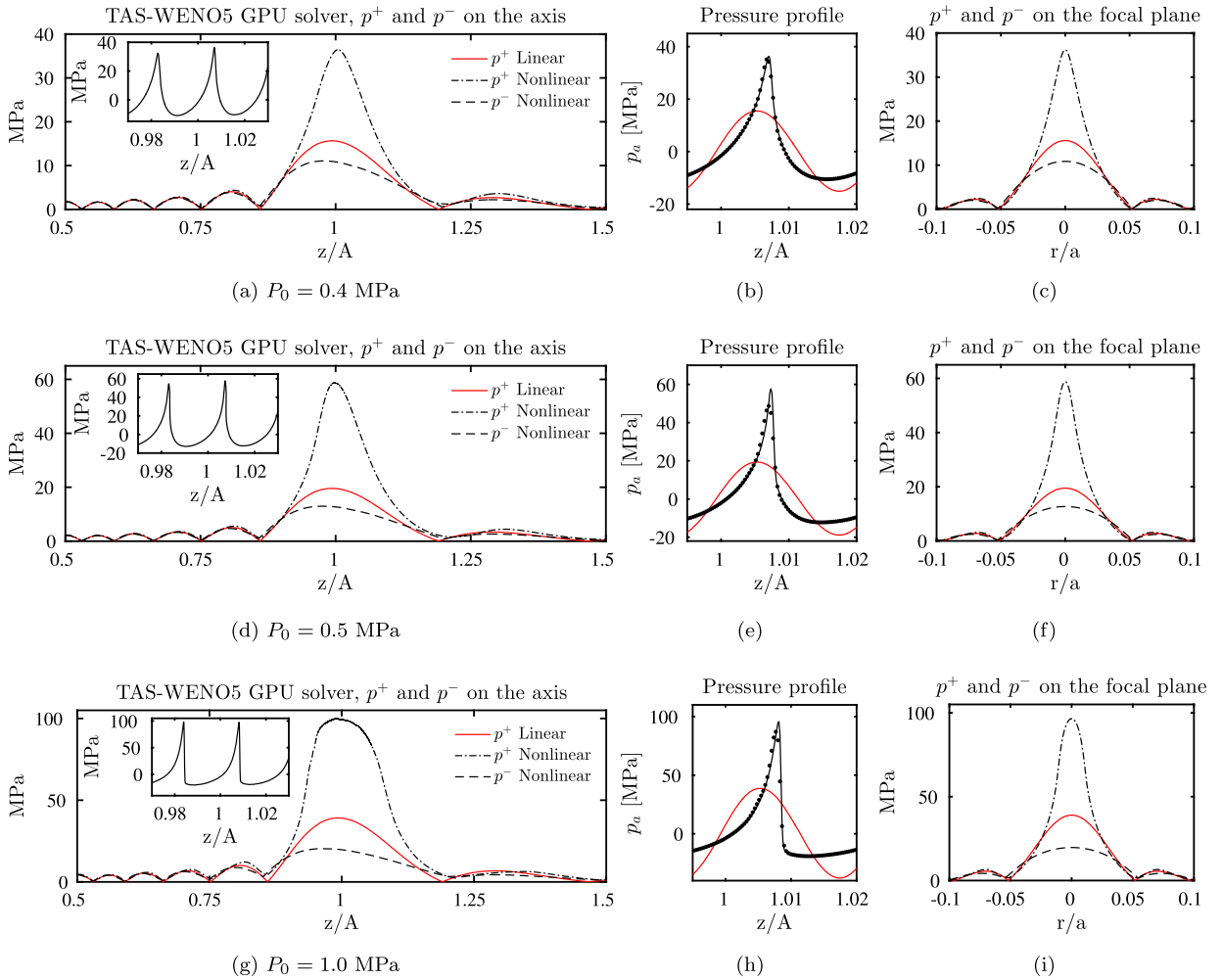
Fig. 13. Weak nonlinear descriptions of a HIFU device: focal distance of $A = 62.6$ mm, aperture of $a = 32$ mm, obtained with a TAS-WENO5 solver and an explicit FDTD Westervelt solver. In (a), (c) and (e), the acoustic pressure distributions at the axis of symmetry are obtained and compared to the linear expectation. In (b), (d) and (f), the wave profiles are directly contrasted at the final output time $t = 66$ μs. The results of these figures show a good agreement between the nonlinear solvers. More details are presented in the text.

5.3.4. Modeling strongly nonlinear propagation with shocks

Lastly, the TAS model is used to study acoustic propagations with absorption and diffraction effects in homogeneous media for strongly nonlinear regimes. As a continuation of the previous test, the properties for degassed water are kept, and we simply study the cases where a sinusoidal acoustic perturbation with a large amplitude, namely $P_0 = 0.4$, 0.45, 0.5 and 1 MPa, is introduced into the system. As before, the computation was performed in a CUDA-C implementation and run on a Tesla K20c GPU unit.

A TAS-WENO5 scheme is initially chosen to evolve the TAS system in each case. In this study shocks are expected to develop during the evolution of the system. As before, a grid with $\Delta x = \Delta y = 2\text{E}{-}5$ m is initially considered. The spanned domain then contains $2\,001 \times 5\,501$ nodes. To ensure accuracy a fixed time step of $\Delta t = 2$ ns is selected. The system is evolved up to time $t = 66$ μs so it requires 33,000 time steps to obtain the solution of each case. The average computation time took about 3.3 hours using a direct GPU implementation. The details on the implementation are reported in Appendix A. The solutions obtained with this resolution are not as sharp as expected. Therefore, they are re-run and solved on a mesh with resolution of $\Delta x = \Delta y = 1\text{E}{-}5$ m. The spanned domain now contains $4\,001 \times 11\,001$ nodes. For this grid 3345 nodes are selected as point sources to represent the discrete profile of the focused device. To ensure the accuracy of the method, a fixed time step of $\Delta t = 1$ ns is selected. The system is evolved up to time $t = 66$ μs, i.e. requiring the solution of 66,000 iterations. For each case, the average computation time took about 25.2 hours using our TAS-WENO5 GPU implementation. The profiles for p^+ and p^- obtained for the propagations of 0.4, 0.5 and 1 MPa are reported in Fig. 14.

The verification of the solutions obtained for P_0: 0.05 to 0.5 MPa is performed by comparing the pressure values at geometrical focal points from the computed solutions with those obtained in experimental measurements in [35] where a device with similar parameters was studied. In Fig. 15, the solutions of the previous section with the TAS-FD5 solver and the solutions of this section with the TAS-WENO5 solver are summarized. Here, the values of p^+ and $|p^-|$ at the geometrical

Fig. 14. Strong nonlinear wave descriptions of a HIFU device: focal distance of $A = 62.6$ mm, aperture of $a = 32$ mm, obtained with the TAS-WENO5 solver. In figures (a), (d) and (g), the acoustic pressure distributions on the axis of symmetry corresponding to a transducer with $P_0 = 0.4$, 0.5 and 1 MPa are depicted. In (b), (e) and (h), the corresponding acoustic pressure profiles along the axis of symmetry are presented. The solid line solution is obtain on a grid with $\Delta x = \Delta y = 1\text{E}{-}5$ m, while the dots correspond to a solution on a grid with $\Delta x = \Delta y = 2\text{E}{-}5$ m. Lastly, in (c), (f) and (i), the respective pressure distributions on the geometrical focal plane (a perpendicular plane at $z/A = 1$) are reported.

focal point of the domain are taken and plotted with respect to P_0 and they are compared to those reported in [35]. The results show that the TAS-FD5 and TAS-WENO5 solutions for the propagations in degassed water match directly without any filtering or averaging technique to the reported measurements. Although this was expected for the smooth solutions, this is achieved satisfactorily for the strongly nonlinear propagation with shocks.

To validate the solution for $P_0 = 1$ MPa, we re-run again this problem using our TAS-WENO7 GPU solver for the refined mesh of $4\,001 \times 11\,001$ nodes. For this cases, the average computation time for this models took 47.6 hours using a TAS-WENO7 GPU implementation. Compared to the computation time with TAS-WENO5, the TAS-WENO7 solver required $1.7\times$ more computation time. This is expected as we use a RK4(5) time integration scheme. However, the TAS-WENO7 solution provides a much sharper result and here is used as a reference solution for this test. The wave profiles of the solutions obtained with TAS-WENO5 and TAS-WENO7 are compared in Fig. 16. As expected, the comparison shows that the numerical results of both models are converging for the shocks structures in the solution. Moreover, it is easy to notice that the shape of the wave starts to approach the profile typically observed in a *shock wave lithotripsy* procedure.

Lastly, the acoustic pressure fields p^+, p^- and the magnitude of the velocity, $|\mathbf{u}_a|$ are computed for a linear propagation and for the present thermoviscous case. Both cases corresponding to a focused device with $P_0 = 1$ MPa propagation in degassed water and solved with the TAS-WENO7. In Fig. 17, the fields are depicted in the vicinity of the geometrical focal point, where it provides a clear contrast between the patterns exhibited by the linear and strongly nonlinear propagation with shocks.

Based on the above results it is clear that a TAS-WENO7 solver provides the sharpest solutions presented in this work. However, the TAS-WENO5 solver provides a good balance between accuracy and computation time. Therefore, TAS-WENO5
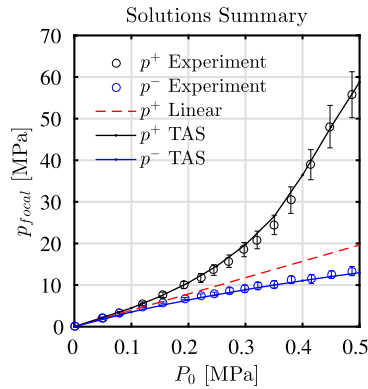
Fig. 15. Pressure magnitude at the geometrical focal point as a function of the input signal amplitude, P_0. These results were obtained by modeling a HIFU device: focal distance of $A = 62.6$ mm, aperture $a = 32$ mm, in linear and nonlinear regimes. The nonlinear solutions reported for an input below $P_0 = 0.35$ MPa were obtained with a TAS-FD5, the rest were obtained with the TAS-WENO5 scheme. These solutions are compared to the experimental data reported in [35]. The result of this test exhibits a good agreement with the physical expectations. More details are provided in the text.
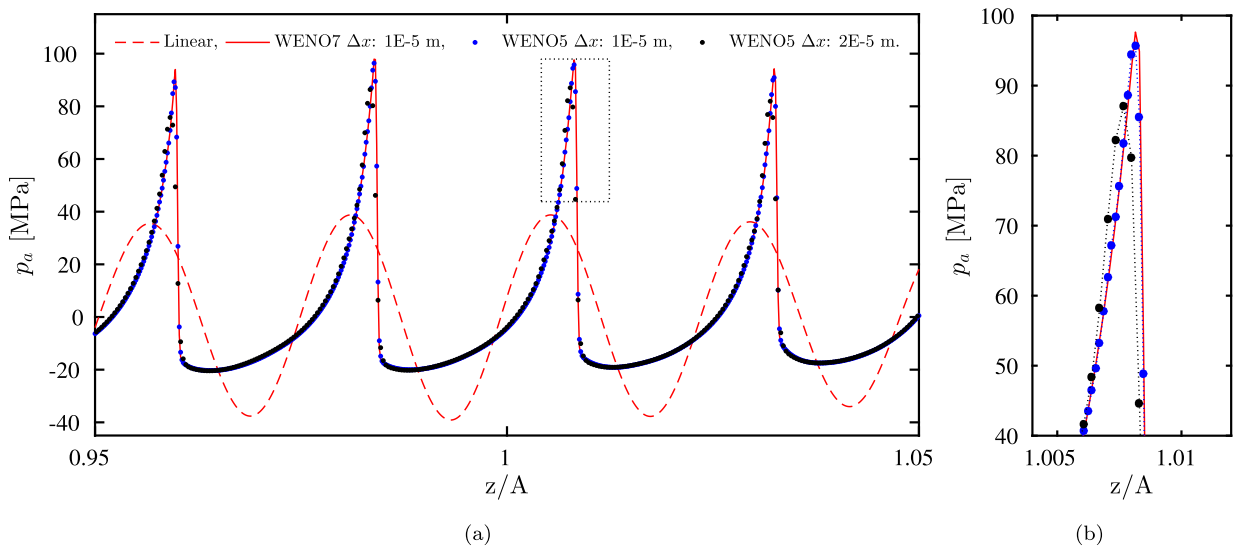
Fig. 16. Pressure wave profiles obtained by modeling a HIFU transducer device: focal distance $A = 62.6$ mm, aperture $a = 32$ mm, with a TAS-WENO5 and a TAS-WENO7 solver for different mesh sizes. All solutions correspond to an input signal of amplitude $P_0 = 1$ MPa at the final time $t = 66$ μs. In analogy to the 1-d mesh refinement test, the results in figures (a)–(b) depict that the method converges to the shock profile. More details are provided in the text.

solver is considered as a suitable numerical scheme for modeling strongly nonlinear propagation in thermoviscous media in higher dimensions.

6. Concluding remarks

In this work, a conservative thermoviscous formulation to describe nonlinear acoustic propagation has been obtained. Moreover, it is found that at the core of this formulation there is a fully nonlinear hyperbolic system, denominated as the *nonlinear acoustic system* of equations.

Like the traditional second-order acoustic formulations, the present formulation solves directly for the acoustic pressure field. However, the present hyperbolic formulation also requires solving for the velocity fields. Nevertheless, the conservative nature of the present formulations makes it suitable to be implemented and solved using traditional high-order shock capturing schemes in the literature, allowing to study strongly nonlinear propagations with shocks directly and without requiring any numerical artifact to filter or damp any spurious oscillations.

This nonlinear hyperbolic system is studied for Cartesian and axisymmetric propagations. Moreover, under the consideration of negligible *nonlinear local effects* the system is found capable of describing classical progressive waves in weak and strong nonlinear regimes and matching the long term inviscid Burgers' shock wave decaying rates. As a thermoviscous model, it is found suitable for the numerical description of nonlinear wave propagation generated by high intensity focused ultrasound (HIFU) devices.
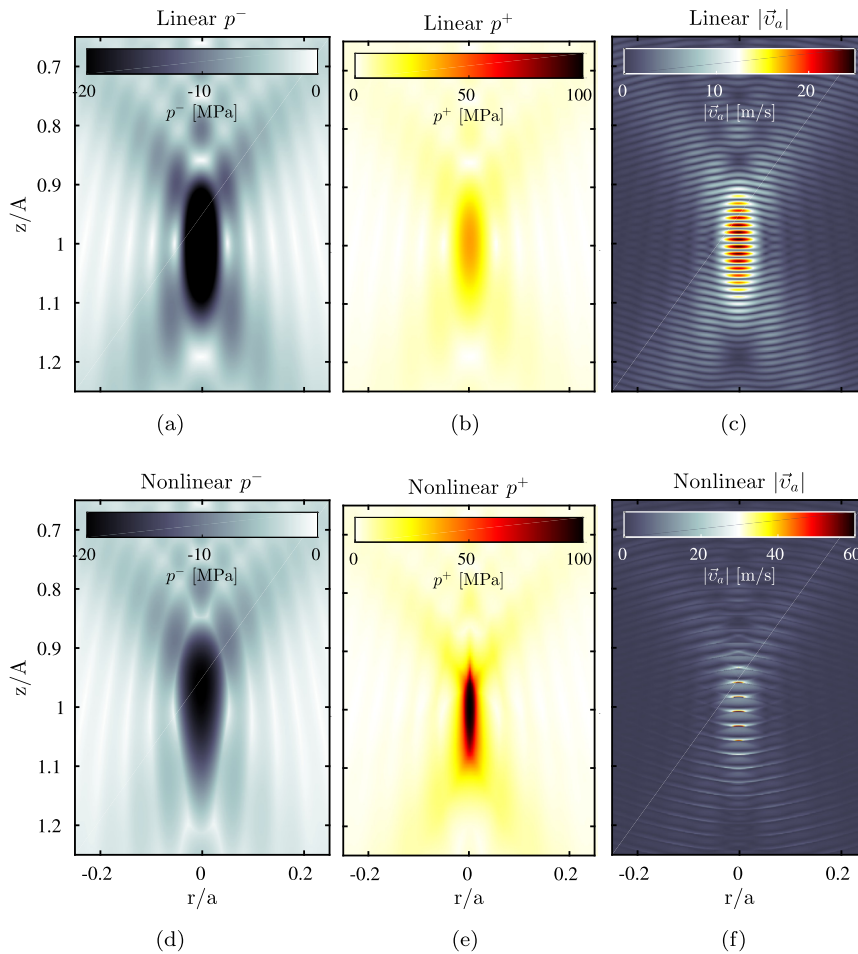
Fig. 17. Positive and negative acoustic pressure distributions, and velocity magnitude field obtained for a focused ultrasound device near the geometrical focal point. The linear fields (a, b, c) were obtained with a TAS-FD7 solver and nonlinear fields (c, d, f) were obtained with a TAS-WENO7 solver. In this test input amplitude is set to $P_0 = 1$ MPa, the focal distance and aperture of the device are $A = 62.6$ mm and $a = 32$ mm, respectively. Digital version is provided in color.

Descriptions of weakly and strongly nonlinear propagations were obtained by means of finite difference WENO reconstructions associated with low-storage Runge–Kutta schemes. The numerical formulation is also found suitable for developing a numerical implementation to be solved on general purpose graphical units (GPUs). When solving for 2-d axisymmetric HIFU tests, CUDA-C implementations of the thermoviscous solver managed to achieve an average performance of 300 Gflop/s. Evidently, the results of this work can be greatly improved, e.g., formulating a multiple-GPU solver to increase performance and reduce computation time, introducing mesh refinement strategies, or further exploring thermoviscous propagations with high-order spectral methods developed for convection–diffusion dominated problems. However, more theoretical understanding would be also desirable.

Let us simply remark that the main interest of this work was to study the conservative thermoviscous formulation and its inviscid simplification, which to our surprise, performed well beyond initial expectations in the numerical experiments. Therefore, we report that two extensions of this work are currently in preparation, namely, an extension of the model for describing propagations is thermoviscous heterogeneous media and a study on the contributions of *local nonlinear effects*. Both extensions will be reported elsewhere.

Acknowledgements

Appendix A. Computer implementation

A CUDA-C numerical implementation with a MATLAB interface was developed to solve for Eq. (86) using general purpose graphical procession units (GPGPUs). The finite difference polynomial and WENO reconstruction algorithms, described in Appendix G, were implemented and optimized to ensure data sharing and maximum data reuse at the time of the computation of the stencils. By using the proposed Runge–Kutta schemes in section 4.1.4, each algorithm only requires storing 3 arrays per acoustic field during the computation time. Namely, the present time step, q^n, the temporal array, $q^{(i)}$, and the discrete spatial operator array, L(q). Tesla K20c GPUs were used for computing all the HIFU examples reported. Each GPU unit contains 2496 cores that run with a clock at 706 MHz, moreover; each unit is equipped with 5.12 GBs of GDDR5 of random access memory with 5 GHz memory speed.

The memory required for a two-dimensional problem can be estimated as

$$\text{memory usage [GBs]} \approx \frac{12(N_z\,N_r) \times 8\,[\text{bytes}]}{1E6\,[\frac{\text{bytes}}{\text{GBs}}]}, \tag{A.1}$$

where N_r and N_z are the grid sizes in the radial and azimuthal directions, respectively. The coefficient accounts for the storage of 9 fields (1 solution field + 2 temporary fields for each acoustic variable), 1 auxiliary PML field and 2 extra fields for computing and storing p^+ and p^-. For the computational grid of 4001×11001, the problem fits into a single unit. The average performance measured for the TAS-WENO5 and TAS-WENO7 solver were 310 Gflop/s and 280 Gflop/s respectively (using double precision operations). Although both solvers exhibit similar performances, these do not translate into similar computation times. Here the WENO5 requires approximately only 1/2 of the time used by the WENO7 solver. Moreover, the TAS-FDM5 and TAS-FDM7 solvers exhibit shorter computation times by a factor of 2/3 w.r.t. their respective WENO counterpart. This is not surprising since the WENO smooth measurements are never computed. Lastly, it is observed that the maximum performance of the present numerical implementation is limited by the strategy used for computing the convective operations and auxiliary routines that produce element-wise computations. Our future work will focus on improving these aspects.

Appendix B. Transformations

Hamilton and Blackstock [18, chap. 2] have shown that consistent second-order, $O(\varepsilon^2)$, can be simply derived from the linearized acoustic equations, namely

$$\frac{\partial \boldsymbol{v}_a}{\partial t} + \frac{1}{\rho_0}\nabla p_a = 0, \tag{B.1a}$$

$$\frac{\partial p_a}{\partial t} + \rho_0 c_0^2 \nabla \cdot \boldsymbol{v}_a = 0. \tag{B.1b}$$

By scaling (B.1a) by $\boldsymbol{v}_a$ and (B.1b) by p_a, the following partial equations are obtained

$$\frac{1}{2}\frac{\partial v_a^2}{\partial t} + \frac{1}{\rho_0}\boldsymbol{v}_a \cdot \nabla p_a = 0, \tag{B.2a}$$

$$\frac{1}{2}\frac{\partial p_a^2}{\partial t} + \rho_0 c_0^2\, p_a \nabla \cdot \boldsymbol{v}_a = 0, \tag{B.2b}$$

where $v_a^2 = \boldsymbol{v}_a \cdot \boldsymbol{v}_a$. Under the assumption of negligible *local nonlinear effects*, Eq. (11) indicates that $v_a^2 = (\frac{p_a}{\rho_0 c_0})^2$, which allows us to summarize the result of the above equations and obtain the relation

$$\frac{1}{\rho_0 c_0^2}\frac{\partial p_a^2}{\partial t} = -\nabla \cdot (p_a \boldsymbol{v}_a) + O(\varepsilon^3). \tag{B.3}$$

Alternatively, it is found that one can obtain the same result by directly considering the vector identity

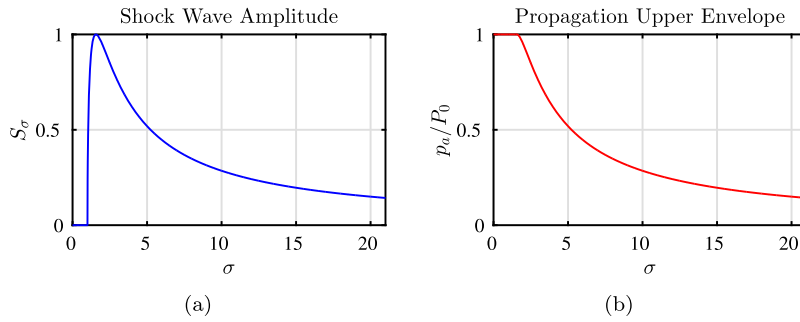$$\nabla \cdot (p_a \boldsymbol{v}_a) = p_a \nabla \cdot \boldsymbol{v}_a + \boldsymbol{v}_a \cdot \nabla p_a \tag{B.4}$$

Following the same principles introduced by Hamilton and Blackstock, the following substitutions can be produced

$$p_a \nabla \cdot \boldsymbol{v}_a = p_a \left(-\frac{1}{\rho_0 c_0}\frac{\partial p_a}{\partial t}\right) = -\frac{1}{2\rho_0 c_0^2}\frac{\partial p_a^2}{\partial t}, \tag{B.5a}$$

$$\boldsymbol{v}_a \cdot \nabla p_a = \boldsymbol{v}_a \cdot \left(-\rho_0 \frac{\partial \boldsymbol{v}_a}{\partial t}\right) = -\frac{\rho_0}{2}\frac{\partial v_a^2}{\partial t} = -\frac{1}{2\rho_0 c_0^2}\frac{\partial p_a^2}{\partial t}. \tag{B.5b}$$

So we arrive to the same conclusion in equation (B.3).

Fig. D.18. In (a) the solution profile of the shock formation problem solved for $\sigma \in [0, 22]$, and (b) the expected wave profile used as a theoretical reference to validate the NAS numerical solution.

Appendix C. Perfect matching layers

In this work, the idea of perfect matching layers (PML) was implemented to study propagations in an open domain. Here, the basic principles of the *complex stretch-coordinate* [28] have been followed. Let us consider the one-dimensional case, as it simply leads to augment the IVP in (38) with the following source term

$$\mathcal{S}(x) = -\sigma_x(x)\boldsymbol{q}. \tag{C.1}$$

Here $\sigma_x(x)$ is an absorption coefficient that is non-zero only inside a sub-region (layer) in the vicinity of the boundary of the domain. The thickness expressed of this layer is $\Delta_{PML} = N\Delta x$, where N is the PML thickness in terms of nodes and Δx is the node interval. For a smooth transition for the region of interest to the boundary layer $\sigma_x(x)$ is defined as the parabolic profile as

$$\sigma_x(x) = \sigma_0 \left(\frac{x}{\Delta_{PML}} \right)^2, \quad \sigma_0 = \log\left(\frac{1}{R} \right) \frac{3V}{2\Delta_{PML}}, \tag{C.2}$$

where V is the propagation speed. Numerical experience shows that it can be safely assumed as $V = c_0$, given that the propagation speed of the linear model dominates the propagation of nonlinear acoustic waves. σ_0 is the maximum damping parameter which is function of the theoretical reflection coefficient R. From [36], the recommended values of R are

$$R = \begin{cases} 0.01 & \text{if } N = 5, \\ 0.001 & \text{if } N = 10, \\ 0.0001 & \text{if } N = 20. \end{cases} \tag{C.3}$$

In this work, PML layers of 20 nodes in thickness were considered in all the benchmark problems studied in section 5.

Appendix D. Theoretical amplitude profile

A theoretical expectation of the amplitude of a sinusoidal wave profile, propagating under the Burgers' model, can be built from the analysis of the formation and decay of a shock wave. Such model has been studied by Blackstock in [33], where it has been shown that the distance to the shock formation, σ, and the amplitude of the shock, S_σ, for a sinusoidal propagation are related by the transcendental equation given by

$$S_\sigma = \sin(\sigma S_\sigma). \tag{D.1}$$

Eq. (D.1) can be numerically solved for S_σ by obtaining the initial that roots emerge for different σ distances. In the σ frame of reference, $\sigma = \pi/2$ corresponds to the position where the shock is fully developed. The numerical solution for S_σ is then depicted in Fig. D.18a. Since the wave amplitude is not altered until the moment that the shock if formed, the expected upper envelope profile is then a slight modification of the shock amplitude profile simply defined as

$$\frac{p_a}{P_0} = \begin{cases} 1 & \text{if } \sigma \leq \pi/2, \\ S_\sigma & \text{if } \sigma > \pi/2. \end{cases} \tag{D.2}$$

Let us remark that for this propagation the upper and lower envelopes of the wave propagation are symmetric with respect to the σ-axis. In Fig. D.18b, the theoretical expectation of the upper envelope of the nonlinear wave propagation is depicted.
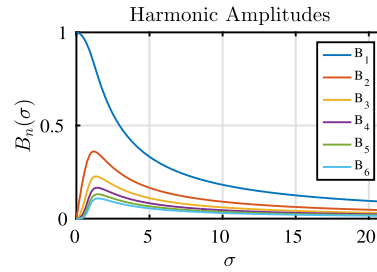
Fig. D.19. Harmonic amplitude profiles.

Appendix E. Inviscid Burgers' classical solutions in time-domain

The knowledge of the theoretical shock amplitude profile motivated Blackstock [33] to devise the missing link between two of the classical solutions of the inviscid Burgers' equation, namely the Fubini and Fay solution. By using σ as a parameter these classical solutions can be summarized as follows

- *Fubini Solution* (Before Shock Solution)

$$\frac{p_a}{P_0} = \sum_{n=1}^{\infty} (2/n\sigma) J_n(n\sigma) \sin(n(\omega t - kx)), \quad \text{for } \sigma < 1 \tag{E.1}$$

- *Blackstock Solution* (The Transition Regime after the Shock Formation)

$$\frac{p_a}{P_0} = \sum_{n=1}^{\infty} B_n \sin(n(\omega t - kx)), \quad \text{for } 1 \leq \sigma < 3.5 \tag{E.2}$$

where

$$B_n(\sigma) = \frac{2}{n\pi} S_\sigma + \frac{2}{n\pi\sigma} \int_{\sigma S_\sigma}^{\pi} \cos(n(\theta - \sigma \sin(\theta)) d\theta. \tag{E.3}$$

Here, S_σ and σ are obtained by numerically solving the Eq. (D.1). The profiles for the first six harmonic functions $B_n(\sigma)$ are plotted in Fig. D.19.

- *Inviscid Fay Solution* (Long Term Solution)

$$\frac{p_a}{P_0} = \sum_{n=1}^{\infty} \frac{2}{n(1+\sigma)} \sin(n(\omega t - kx)), \quad \text{for } \sigma \geq 3.5. \tag{E.4}$$

This result is obtained by letting $\Gamma \to \infty$ in Fay's classical viscous solution.

Notice that by setting $k = 0$ in equations (E.1) to (E.4), it becomes evident that classical wave solutions of the inviscid Burgers' equation are provided as the time domain profiles of the nonlinear progressive wave. To make this comparison we require to create a time history of the propagation by saving the wave profile every single time step at specific σ-distance. Then the expected solution profiles at the selected σ-distances can be computed simply by truncating the summation in Eqs. (E.1), (E.2) and (E.4) to a suitable number of terms.

Appendix F. Solution of the linear focused ultrasound propagation

It is well-known that the acoustic pressure field from a vibrating surface can be described by means of the Rayleigh integral. Although a solution of the Rayleigh integral is exact only for a sound field from a planar source, O'Neil [34] showed that it can be applicable to the beams from a curved radiating source under the assumptions of relatively weak curvature of the source and sufficiently high frequency. Under these assumptions, O'Neil managed to obtain explicit solutions of the wave propagation profiles at the axis of symmetry and in the vicinity of the focal plane.

In this test, we are only interested in the propagation profiles on the axis of symmetry of the transducer. The basic parameters that characterize this profile are: the radius of curvature, A [m], the transducer aperture, a [m], speed of sound in the media c_0 [m/s], and the device frequency f [MHz]. From which the following dependent variables are defined
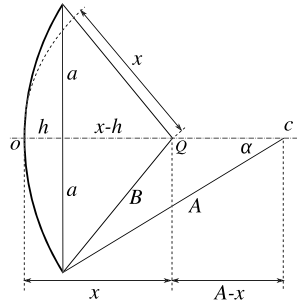
Fig. F.20. Scheme of geometrical parameters used in O'Neil's linear solution.

$$
\begin{cases}
\text{aperture angle} & \alpha = \arcsin(a/A), \\
\text{concavity depth} & h = A/(1 - \cos\alpha), \\
\text{physical wave length} & \lambda = c_0/f, \\
\text{waves per length unit} & k = 2\pi/\lambda, \\
\text{angular frequency} & \omega = 2\pi f.
\end{cases}
$$

Form these parameters and dependent variables, the wave propagation profile at the axis of symmetry is simply given by

$$
p_a = i\, P_0 \, \frac{2\sin(k(B-x)/2)}{1 - x/A} \exp(\omega t - ikM), \tag{F.1}
$$

where P_0 is the input amplitude of the acoustic signal introduced by the device in MPa, M is a function defined as $M = (B + x)/2$, $B = \sqrt{(x-h)^2 + a^2}$ and x represents a point on the axis of symmetry. In this work we will refer to Eq. (F.1) simply as the *O'Neil's solution*. (See Fig. F.20.)

It has been verified that O'Neil's solution induced from the Rayleigh integral has a good applicability for much wider angles of aperture than generally thought. Actually, favorable agreement between the solutions is found for $a_0 < 60$ [deg] and within a range of $ka = 10$ to 50 wavelengths.

Appendix G. Finite difference reconstructions

The reconstruction problem is a special type of interpolation procedure relevant to the approximation of the convective operators. We simply refer to the work of Jiang and Shu in [26] for the details.

G.1. A fifth- and seventh-order polynomial reconstruction

By considering the large stencils $S = \{x_{i-2}, \ldots, x_{i+2}\}$ to interpolate for f^+ values and stencil $S = \{x_{i-1}, \ldots, x_{i+3}\}$ for f^- values. A reconstruction of these interpolating polynomials to approximate the values of f to the right ($+$) and to the left ($-$) of the cell interface $x_{i+1/2}$ yields

$$
\begin{cases}
\hat{f}^+_{i+\frac{1}{2}} = (2f^+_{i-2} - 13f^+_{i-1} + 47f^+_i + 27f^+_{i+1} - 3f^+_{i+2})/60, \\
\hat{f}^-_{i+\frac{1}{2}} = (-3f^-_{i-1} + 27f^-_i + 47f^-_{i+1} - 13f^-_{i+2} + 2f^-_{i+3})/60.
\end{cases}
\tag{G.1}
$$

Both $\hat{f}^+_{i+\frac{1}{2}}$ and $\hat{f}^-_{i+\frac{1}{2}}$ are fifth order accurate

$$
\hat{f}^+_{i+\frac{1}{2}} - f^+(x_{i+\frac{1}{2}}) = O(\Delta x^5), \quad \hat{f}^-_{i+\frac{1}{2}} - f^-(x_{i+\frac{1}{2}}) = O(\Delta x^5).
$$

Similarly, by considering the large stencils $S = \{x_{i-3}, \ldots, x_{i+3}\}$ to interpolate for f^+ values and stencil $S = \{x_{i-2}, \ldots, x_{i+4}\}$ for f^- values. The resulting reconstructed approximations of f to the right and to the left of the cell interface $x_{i+1/2}$ are

$$
\begin{cases}
\hat{f}^+_{i+\frac{1}{2}} = (-3f^+_{i-3} + 25f^+_{i-2} - 101f^+_{i-1} + 319f^+_i + 214f^+_{i+1} - 38f^+_{i+2} + 4f^+_{i+3})/420, \\
\hat{f}^-_{i+\frac{1}{2}} = (4f^-_{i-2} - 38f^-_{i-2} + 214f^-_i + 319f^-_{i+1} - 101f^-_{i+2} + 25f^-_{i+3} - 3f^-_{i+4})/420,
\end{cases}
\tag{G.2}
$$

which are both seventh order accurate.

References

[1] M. Solovchuk, T.W.-H. Sheu, M. Thiriet, Multiphysics modeling of liver tumor ablation by high intensity focused ultrasound, Commun. Comput. Phys. 18 (4) (2015) 1050–1071.
[2] J. Kennedy, G. Ter Haar, D. Cranston, High intensity focused ultrasound: surgery of the future?, Br. J. Radiol. 76 (909) (2003) 590–599.
[3] J.E. Lingeman, J.A. McAteer, E. Gnessin, A.P. Evan, Shock wave lithotripsy: advances in technology and technique, Nat. Rev. Urol. 6 (12) (2009) 660–670.
[4] T.L. Szabo, Diagnostic Ultrasound Imaging: Inside Out, Academic Press, 2004.
[5] P. Jordan, A survey of weakly-nonlinear acoustic models: 1910–2009, Mech. Res. Commun. 73 (2016) 127–139, https://doi.org/10.1016/j.mechrescom.2016.02.014.
[6] I.M. Hallaj, R.O. Cleveland, FDTD simulation of finite-amplitude pressure and temperature fields for biomedical ultrasound, J. Acoust. Soc. Am. 105 (5) (1999) L7–L12.
[7] A. Karamalis, W. Wein, N. Navab, Fast ultrasound image simulation using the Westervelt equation, in: International Conference on Medical Image Computing and Computer-Assisted Intervention, Springer, 2010, pp. 243–250.
[8] A.A. Haigh, B.E. Treeby, E.C. McCreath, Ultrasound simulation on the cell broadband engine using the Westervelt equation, in: International Conference on Algorithms and Architectures for Parallel Processing, Springer, 2012, pp. 241–252.
[9] S. Ginter, M. Liebler, E. Steiger, T. Dreyer, R.E. Riedlinger, Full-wave modeling of therapeutic ultrasound: nonlinear ultrasound propagation in ideal fluids, J. Acoust. Soc. Am. 111 (5) (2002) 2049–2059.
[10] B.E. Treeby, J. Jaros, A.P. Rendell, B. Cox, Modeling nonlinear ultrasound propagation in heterogeneous media with power law absorption using a k-space pseudospectral method, J. Acoust. Soc. Am. 131 (6) (2012) 4324–4336.
[11] N. Albin, O.P. Bruno, A spectral FC solver for the compressible Navier–Stokes equations in general domains, I: Explicit time-stepping, J. Comput. Phys. 230 (16) (2011) 6248–6270.
[12] N. Albin, O.P. Bruno, T.Y. Cheung, R.O. Cleveland, Fourier continuation methods for high-fidelity simulation of nonlinear acoustic beams, J. Acoust. Soc. Am. 132 (4) (2012) 2371–2387.
[13] R.J. LeVeque, Finite Volume Methods for Hyperbolic Problems, vol. 31, Cambridge University Press, 2002.
[14] E.F. Toro, Riemann Solvers and Numerical Methods for Fluid Dynamics: A Practical Introduction, Springer Science & Business Media, 2013.
[15] I. Christov, P. Jordan, C. Christov, Nonlinear acoustic propagation in homentropic perfect gases: a numerical study, Phys. Lett. A 353 (4) (2006) 273–280.
[16] I. Christov, C. Christov, P. Jordan, Modeling weakly nonlinear acoustic wave propagation, Q. J. Mech. Appl. Math. 60 (4) (2007) 473–495.
[17] S.I. Aanonsen, T. Barkve, J.N. Tjøtta, et al., Distortion and harmonic generation in the nearfield of a finite amplitude sound beam, J. Acoust. Soc. Am. 75 (3) (1984) 749–768.
[18] M.F. Hamilton, D.T. Blackstock, et al., Nonlinear Acoustics, vol. 427, Academic Press, San Diego, 1998.
[19] R.O. Cleveland, Propagation of Sonic Booms through a Real, Stratified Atmosphere, Ph.D. thesis, The University of Texas at Austin, 1995.
[20] P.J. Westervelt, Parametric acoustic array, J. Acoust. Soc. Am. 35 (4) (1963) 535–537.
[21] J.M. Burgers, A mathematical model illustrating the theory of turbulence, Adv. Appl. Mech. 1 (1948) 171–199.
[22] J.-P. Berenger, A perfectly matched layer for the absorption of electromagnetic waves, J. Comput. Phys. 114 (2) (1994) 185–200.
[23] N.A. Petersson, O. O'Reilly, B. Sjögreen, S. Bydlon, Discretizing singular point sources in hyperbolic wave propagation problems, J. Comput. Phys. 321 (2016) 532–555.
[24] C.-W. Shu, S. Osher, Efficient implementation of essentially non-oscillatory shock-capturing schemes, J. Comput. Phys. 77 (2) (1988) 439–471.
[25] M. Carpenter, C. Kennedy, Fourth-order 2N-storage Runge–Kutta schemes, NASA TM-109112, National Aeronautics and Space Administration, Langley Research Center, Hampton, VA, 1994.
[26] G.-S. Jiang, C.-W. Shu, Efficient implementation of weighted ENO schemes, J. Comput. Phys. 126 (1) (1996) 202–228.
[27] D.S. Balsara, C.-W. Shu, Monotonicity preserving weighted essentially non-oscillatory schemes with increasingly high order of accuracy, J. Comput. Phys. 160 (2) (2000) 405–452.
[28] S.G. Johnson, Notes on Perfectly Matched Layers (PMLs), Lecture notes, 5 (5.3), Massachusetts Institute of Technology, Massachusetts, 2008, p. 2.
[29] M.A. Diaz, M.-H. Chen, J.-Y. Yang, High-order conservative asymptotic-preserving schemes for modeling rarefied gas dynamical flows with Boltzmann-BGK equation, Commun. Comput. Phys. 18 (4) (2015) 1012–1049.
[30] M.A. Diaz, J.-Y. Yang, An efficient direct solver for rarefied gas flows with arbitrary statistics, J. Comput. Phys. 305 (2016) 127–149.
[31] M. Solovchuk, T.W. Sheu, M. Thiriet, Simulation of nonlinear Westervelt equation for the investigation of acoustic streaming and nonlinear propagation effects, J. Acoust. Soc. Am. 134 (5) (2013) 3931–3942.
[32] Y. Shen, G. Zha, A robust seventh-order WENO scheme and its applications, in: 46th AIAA Aerospace Sciences Meeting and Exhibit, 2008, p. 757.
[33] D.T. Blackstock, Connection between the Fay and Fubini solutions for plane sound waves of finite amplitude, J. Acoust. Soc. Am. 39 (6) (1966) 1019–1026.
[34] H. O'Neil, Theory of focusing radiators, J. Acoust. Soc. Am. 21 (5) (1949) 516–526.
[35] O.V. Bessonova, V. Wilkens, Membrane hydrophone measurement and numerical simulation of HIFU fields up to developed shock regimes, IEEE Trans. Ultrason. Ferroelectr. Freq. Control 60 (2) (2013) 290–300.
[36] F. Collino, C. Tsogka, Application of the perfectly matched absorbing layer model to the linear elastodynamic problem in anisotropic heterogeneous media, Geophysics 66 (1) (2001) 294–307.